On the Use of a Two-Dimensional Cyclic Prefix in OTFS Modulation and its Implications

Michele Mirabella [1], Pasquale Di Viesti[1], and Giorgio M Vitetta[1]

[1]Affiliation not available

March 14, 2024

On the Use of a Two-Dimensional Cyclic Prefix in OTFS Modulation and its Implications

Michele Mirabella, *Graduate Student Member, IEEE* Pasquale Di Viesti, *Graduate Student Member, IEEE* and Giorgio M. Vitetta, *Senior Member, IEEE*

Abstract

In this manuscript we investigate the implications of adopting a double cyclic prefix in the orthogonal time-frequency space modulation. Our study first focuses on the analysis of the modulated signal and on the development of a useful model for the received signal in the presence of a doubly selective fading channel. On the one hand, our mathematical results allow us to accurately assess the impact of pulse shaping on the structure of the transmitted waveform and on its power spectral density, and to develop some simple rules for allocating multiple pilot symbols within each orthogonal time-frequency space symbol. On the other hand, they are exploited to develop a novel algorithm for pilot-aided channel estimation, whose output provides a detailed representation of the communication channel; for this reason, it can be used for sensing at the transmit side in integrated sensing and communication applications, or for channel equalization at the receive side in digital communications. Our numerical results evidence that our channel estimation & equalization algorithm outperforms the other related techniques available in the technical literature at the price of a limited increase in computational complexity.

Index Terms

Channel Estimation, Cyclic Prefix, Delay-Doppler, Equalization, Interference, Orthogonal Frequency-Division Multiplexing, Orthogonal Time-Frequency Space

I. INTRODUCTION

IN the near future, *sixth-generation* (6G) wireless networks are expected to provide high-quality wireless connectivity as well as highly accurate and robust sensing capability. One of the key challenges in 6G network research is represented by the development of new communication waveforms that are able to support communication and sensing functionalities in high-mobility environments at very high frequencies. In the last two decades, a multicarrier modulation format, known *orthogonal frequency-division multiplexing* (OFDM), has played a fundamental role in new standards for local area and mobile wireless networks. Recently, substantial efforts have been devoted to investigating its use for *integrated sensing and communication* (ISAC) in future wireless networks [1], [2]. Unluckily, one of the main weaknesses of OFDM-based data communications is represented by the severe *inter-carrier interference* (ICI) experienced at the *receive* (RX) side in the presence of a doubly selective fading channel characterized by strong Doppler [3]. From this perspective, a more appealing alternative is represented by a *two-dimensional* (2D) modulation technique called *orthogonal time-frequency space* (OTFS) modulation [4]. In fact, it has been shown that, since in this case data are modulated in the *delay-Doppler* (DD) domain rather than in the conventional *time-frequency* (TF) domain, the communication channel has approximately the same impact on all the channel symbols of the same OTFS symbol and its full diversity can be potentially extracted through proper equalization methods [5].

It is important to mention that *Hadani et al.*, in their seminal manuscript [4], presented the OTFS modulation as a 2D generalization of the OFDM format, but did not focus on the problem of adopting, in a similar way as OFDM, a proper *cyclic prefix* (CP) to impart a quasi-periodic structure to the transmitted signal; this issue has been also ignored in their later manuscript [5]. Note that the presence of a CP plays a fundamental role in the generation of OFDM signals and in their detection over frequency selective (i.e., time dispersive) communications channels, and eliminates interference between consecutive OFDM symbols [6, Sec. 3.7]. Moreover, since the OTFS modulation generalizes OFDM by expanding the last format along the frequency dimension, in the light of the TF *duality principle* [7], the use of an additional CP in that dimension in the presence of a frequency dispersive communication channel appears to be a natural choice.

As far as we know, the use of a CP in the OTFS modulation has been taken into consideration for the first time in [8], [9] and, later, in [10]. In all these manuscripts, however, the CP is adopted *along the time dimension*

only. When this occurs, interference between OTFS symbols (i.e., *inter-symbol interference*, ISI) is avoided if the CP is long enough [11]; otherwise, this phenomenon has to be taken into account in the received signal model [12], [13]). Another significant contribution related to the CP issue can be found in [10], where a derivation of the OTFS modulation based on the Zak transform [14] is provided. The use of this transform makes an entire OTFS frame appear periodic to the communication channel along the Doppler direction and "quasi-periodic" along the delay direction. This work effectively encompasses the concept of imparting 2D periodicity to the modulated signal. However, in our opinion, it does not fully unveil the implications of the use of a CP along the frequency dimension.

In this manuscript, we focus on the use of a *double cyclic prefix* (DCP) in the OTFS modulation and on its implications on pulse shaping and pilot-aided channel estimation. More specifically, the following contributions are provided:

1) It is shown that the OTFS modulation can be really developed as a 2D extension of the OFDM modulation by exploiting the *duality concept* developed by *Bello* in [7]. This leads to extending OTFS symbols by incorporating a CP in the *time domain* (TD) and one in the *frequency domain* (FD) in a natural fashion; the resulting modulation format is called OTFS with DCP (OTFS-DCP, briefly) in the following.

2) The impact of the *transmit* (TX) pulse on the overall structure of the modulated signal is assessed in a rigorous way. Our analysis is based on representing the complex envelope of an OTFS-DCP signal and its spectrum through their Fourier series; the adoption of this mathematical tool is made possible by the cyclic structure of the modulated signal along the time and the frequency dimensions. Note that, in the technical literature, a rectangular TX pulse is usually selected because of its simplicity and the simplifications it offers in signal modelling (e.g., see [8], [9], [13], [15]–[17]). We show, instead, that the choice of a pulse having a *root* of a *raised cosine* (RRC) spectrum represents a better choice.

3) The *power spectral density* (PSD) of the OTFS-DCP format is derived and analyzed.

4) The problem of multiple pilot arrangement within a single OTFS symbol is studied and a specific solution is developed.

5) A low complexity off-grid algorithm, developed for OFDM-based radar sensing [18], is applied to pilot-aided channel estimation in OTFS-DCP-based transmissions. This algorithm is able to generate a detailed representation of the communication channel by providing estimates of its overall number of paths and, for each path, the associated delay and Doppler shift. For this reason, its output can be used for sensing (i.e., for target detection and estimation [16], [17]) at the TX side and for channel equalization at the RX side.

6) A simple channel equalization method relying on the output of the devised channel estimator is developed. This algorithm is inspired by the equalization method proposed in [17], where, however, *channel state information* (CSI) are provided in an approximate form since only integer delays and Doppler are assumed in its reconstruction. On the contrary, our method aims at faithfully reconstructing CSI.

The remaining part of this manuscript is organized as follows. Section II is devoted to briefly describing OFDM and its dual modulation scheme, and to showing how the OTFS-DCP format is related to them. In the analysis of the OTFS modulation format, we take into consideration not only the baseband model of the transmitted signal, but also show how channel equalization and detection of channel symbols should be accomplished at the RX side. Moreover, the impact of pulse shaping on the inner structure of the OTFS-DCP format and its PSD are investigated. Section III is devoted to pilot-aided channel estimation and to channel equalization. In particular, we first provide some simple rules for arranging multiple pilots within a single OTFS symbol under the assumption that a pulse with an RRC spectrum is employed. Then, we show how computationally efficient channel estimation and equalization algorithms can be developed for the OTFS-DCP modulation. Finally, we compare the devised algorithms with two related techniques available in the technical literature. Various numerical results are illustrated in Section IV, where the performance of our channel estimation & equalization algorithms is assessed and compared with that provided by the other algorithms considered in the previous section. Finally, some conclusions are offered in Section V.

Notation: Throughout this paper, the following notation is adopted: 1) $(\cdot)^T$ denotes vector/matrix transposition; 2) $(\cdot)^*$ and $(\cdot)^H$ denote complex conjugate and complex conjugate transpose (Hermitian operator), respectively; 3) $*$ denote the linear convolution; 4) the symbols $\odot$ and $\times$ represent the Hadamard and Cartesian product operators, respectively; 5) $R_N[\cdot]$ indicates the *modulo N operator*; 6) $\boldsymbol{\Xi}_X$ is the unitary DFT matrix of order X, whose element (p, q) is $\exp(-j2\pi pq/X)/\sqrt{X}$; 7) $\mathbf{X} \triangleq [x_{m,n}]$ defines a matrix $\mathbf{X}$ of proper size and $x_{m,n}$ denotes the element appearing on its mth row and nth column.

II. SIGNAL AND SYSTEM MODELS

In this section, we illustrate: 1) the derivation of three distinct digital modulations; 2) the signal models at the RX side of a communication system employing each of these modulations and operating in the presence of different types of fading channels. First, we briefly describe how an OFDM signal is generated and derive the corresponding RX signal model in the presence of a *frequency selective* fading channel. Then, following the same line of reasoning and applying the duality concept, we introduce the dual of the OFDM format (briefly, *dual* OFDM, DOFDM) and develop the corresponding RX signal model in the presence of a *time selective* fading channel. Finally, we show how the signal model of the OTFS-DCP modulation can be derived from most of the previously obtained results in a natural fashion; moreover, we develop the received signal model for a communication system employing that modulation format and operating over a *doubly selective* fading channel.

A. Signal Models in an OFDM-Based Communication System

In this subsection, the derivation of various signal models is sketched for a communication system employing the OFDM modulation. In our mathematical developments we focus on the transmission of the N-dimensional vector $\mathbf{c}_N \triangleq [c_0, c_1, ..., c_{N-1}]^T$, representing the message and collecting N *channel symbols*, each of which belongs to an $M_c$ary constellation; this vector represents a single OFDM *symbol*. To begin, we assume that $\mathbf{c}_N$ undergoes the one-to-one transformation $\mathbf{g} : \mathbb{C}^N \to \mathbb{C}^N$; this yields the N-dimensional vector

$$\mathbf{x}_N \triangleq [x_0, x_1, ..., x_{N-1}]^T = \mathbf{g}(\mathbf{c}_N) \tag{1}$$

conveying the same information as $\mathbf{c}_N$. The last vector is employed to generate the periodic sequence $\{x_k\}$ by repeating it with period N, so that

$$x_k = x_{R_N[k]}, \tag{2}$$

for any $k \notin \{0, 1, ..., N-1\}$. This sequence feeds a pulse amplitude modulator, that produces the baseband periodic signal

$$s(t; \mathbf{c}_N) = \sum_{k=-\infty}^{+\infty} x_k \, p(t - kT_s), \tag{3}$$

where $p(t)$ is the *modulator impulse response* and T_s is the *symbol interval*. Since the period of $s(t; \mathbf{c}_N)$ in (3) is $T = NT_s$, this signal can be represented through its Fourier series as

$$s(t; \mathbf{c}_N) = \sum_{m=-\infty}^{+\infty} S_m^{(\mathrm{TD})}(\mathbf{c}_N) \exp(j2\pi f_m t), \tag{4}$$

where $f_m \triangleq m/T = m/(NT_s)$ is the mth harmonic frequency and

$$S_m^{(\mathrm{TD})}(\mathbf{c}_N) \triangleq \frac{1}{T} \int_0^T s(t; \mathbf{c}_N) \exp(-j2\pi f_m t) dt \tag{5}$$

is the mth Fourier coefficient. Substituting the *right-hand side* (RHS) of (3) in that of (5) yields, after some manipulation,

$$S_m^{(\mathrm{TD})}(\mathbf{c}_N) = \frac{1}{\sqrt{NT_s}} P_m \, X_m, \tag{6}$$

for any m; here,

$$P_m = P(f_m) = P\left(\frac{m}{NT_s}\right), \tag{7}$$

$$P(f) = \mathrm{FCT}[p(t)] \triangleq \int_{-\infty}^{+\infty} p(t) \exp(-j2\pi f t) dt \tag{8}$$

is the *Fourier continuous transform* (FCT) of $p(t)$ and

$$X_m \triangleq \frac{1}{\sqrt{N}} \sum_{l=0}^{N-1} x_l \exp\left(-j2\pi \frac{l}{N} m\right) \tag{9}$$

is the mth coefficient of the order N *discrete Fourier transform* (DFT) of the vector $\mathbf{x}_N$, in (1). Note that the last equation can be rewritten in vector form as

$$\mathbf{X}_N \triangleq [X_0, X_1, ..., X_{N-1}]^T \triangleq \text{DFT}_N[\mathbf{x}_N] \triangleq \mathbf{\Xi}_N\, \mathbf{x}_N, \tag{10}$$

where $\mathbf{\Xi}_N$ is the order N DFT matrix. Then, if the transformation $\mathbf{g}(\cdot)$ in (1) is an order N *inverse discrete Fourier transform* (IDFT), i.e., if

$$\mathbf{x}_N = \text{IDFT}_N[\mathbf{c}_N] \triangleq \mathbf{\Xi}_N^H \mathbf{c}_N, \tag{11}$$

we have that (see (10))

$$\mathbf{X}_N = \mathbf{\Xi}_N \mathbf{\Xi}_N^H \mathbf{c}_N = \mathbf{c}_N. \tag{12}$$

Similarly as $\mathbf{x}_N$, $\mathbf{X}_N$ can be cyclically extended to generate the periodic sequence $\{X_k\}$, having period equal to N; from (12) it is easily inferred that

$$X_k = c_{R_N[k]} \tag{13}$$

for any $k \notin \{0, 1, ..., N-1\}$. Substituting the RHS of (13) in that of (6) and, then, the resulting expression in the RHS of (4) yields

$$s(t; \mathbf{c}_N) = \frac{1}{\sqrt{N T_s}} \sum_{m=-\infty}^{+\infty} P_m\, c_{R_N[m]} \exp(j2\pi f_m t). \tag{14}$$

The last expression can be reformulated by replacing the (single) index m with the couple (n, k), such that $m = n + kN$, with $n = 0, 1, ..., N-1$ and k arbitrary integer. This produces

$$s(t; \mathbf{c}_N) = \frac{1}{\sqrt{N T_s}} \sum_{n=0}^{N-1} c_n\, g_n(t), \tag{15}$$

where

$$g_n(t) \triangleq \sum_{k=-\infty}^{+\infty} P_{n+kN} \exp(j2\pi f_{n+kN}\, t). \tag{16}$$

The RHS of (15) is required to represent a multicarrier signal, i.e., to consist of the superposition of N complex exponentials, characterized by distinct frequencies, having the same amplitude and conveying different channel symbols. This result is achieved if only a single term and, in particular, the one associated with $k = 0$, survives in the sum appearing in the RHS of (16), i.e., if $P_{n+kN} = 0$ for any $k \neq 0$; this means that $p(t)$ should be bandlimited and its spectrum $P(f)$ should ensure that the spectral samples $\{P_n; n = 0, 1, ..., N-1\}$ are identical. In [6, Subsec. 3.7] it is shown that a good option for $p(t)$ is represented by a pulse whose spectrum $P(f)$ is the RRC[1] with *roll-off* factor α (e.g., see [6, Subsect. 3.5.4, eq. (3.90)])

$$P(f) = \begin{cases} \sqrt{T_s} & |f| < f_{1-\alpha} \\ \sqrt{T_s} \cos\left(\pi \frac{|2fT_s|-1+\alpha}{4\alpha}\right) & f_{1-\alpha} \le |f| \le f_{1+\alpha}, \\ 0 & |f| > f_{1+\alpha} \end{cases} \tag{17}$$

where $f_{1\pm\alpha} \triangleq (1 \pm \alpha)/(2T_s)$, with $0 \le \alpha \le 1$. However, in this case, the contribution of some of the functions $\{g_n(t)\}$ appearing in the RHS of (15) needs to be *suppressed*, since they consist of the superposition of a *couple*[2] of complex exponentials, whose frequencies are spaced apart by $1/T_s$ Hz (see [6, Sebsect. 3.7.2, eq. (3.257)]). The suppression of such functions is obtained by setting $N_{sc} \triangleq N - 2N_\alpha - 1$ consecutive elements of $\mathbf{c}_N$ (and, in particular, the elements whose index runs from N_α to $N - N_\alpha - 1$) to zero; here,

$$N_\alpha \triangleq \left\lfloor \frac{N(1-\alpha)}{2} \right\rfloor, \tag{18}$$

---

[1]This spectrum is characterized by a flat top; the identical spectral samples $\{P_n\}$ originate from it.

[2]If subcarrier suppression was not used, this would result in the presence of a form of self-interference.

where $\lfloor \cdot \rfloor$ denotes the *floor* operator. Then, (15) turns into

$$s(t; \mathbf{c}_N) = \frac{1}{\sqrt{NT_s}} \sum_{n=-N_\alpha}^{N_\alpha} c_{R_N[n]} \exp(j2\pi f_n t). \tag{19}$$

Note that: 1) in the last equation, $c_{R_N[n]} = c_n$ for $n = 0, 1, ..., N_\alpha$ and $c_{R_N[n]} = c_{N+n}$ for $n = -N_\alpha, -N_\alpha+1, ..., -1$; 2) the number of *useful subcarriers* is equal to $N_u = 2N_\alpha + 1$ and increases as the roll-off factor gets closer to zero at the price of a longer $p(t)$; 3) the number of *suppressed carriers* (SCs) is equal to $N - N_u$; 4) the subcarrier spacing is equal to $1/(NT_s)$; 5) the pulse $p(t)$ characterized by the spectrum $P(f)$ (17) is truncated to L_p symbol intervals (where L_p is an integer parameter) to ensure that the transmission of each OFDM symbol is accomplished over a finite time interval; 6) since the truncation interval adopted for $p(t)$ is required to capture most of the energy of this pulse, its duration should increase as α gets smaller.

Let us assume now that the signal $s(t; \mathbf{c}_N)$ (19) is sent over a time-invariant frequency selective wireless channel having impulse response

$$h(\tau) \triangleq \sum_{l=0}^{L-1} h_l \delta(\tau - \tau_l), \tag{20}$$

where h_l and τ_l represent the complex gain and the delay, respectively, of the lth path, with $l = 0, 1, ..., L-1$, and L is the number of multi-path components. The useful component of the baseband signal available at the output of the RX filter can be written as

$$r(t; \mathbf{c}_N) \triangleq s(t; \mathbf{c}_N) * h(t) * g(t), \tag{21}$$

where $g(t)$ represents the impulse response of the RX filter, which is assumed to be *matched*[3] to $p(t)$ (i.e., $g(t) = p^*(-t)$), so that $G(f) \triangleq \text{FCT}[g(t)] = P^*(f)$. Then, under this assumption, substituting the RHS of (19) in that of (21) produces

$$r(t; \mathbf{c}_N) = \frac{1}{\sqrt{N}} \sum_{n=-N_\alpha}^{N_\alpha} c_{R_N[n]} H_{R_N[n]} \exp(j2\pi f_n t), \tag{22}$$

where $H_n \triangleq H(f_n)$ and $H(f) \triangleq \text{FCT}[h(t)]$. Note that, if (20) holds, we have that

$$H(f) = \sum_{l=0}^{L-1} h_l \exp(-j2\pi f \tau_l), \tag{23}$$

Comparing (22) with (19) leads to the conclusion that: 1) $r(t; \mathbf{c}_N)$ retains the same structure as the signal feeding the channel input; 2) the effect of the communication channel on the nth subcarrier of the transmitted signal is represented by the complex coefficient $H_{R_N[n]}$. Moreover, given $r(t; \mathbf{c}_N)$ in (22), the extraction of the transmitted message requires: a) uniformly sampling this signal N times in the interval $[0, NT_s]$; b) evaluating an order N DFT on the resulting sample vector; c) compensating for channel distortion on a subcarrier-by-subcarrier basis (i.e., *equalizing* the received signal in the FD); d) accomplishing symbol detection the basis of the equalized samples (once again, on a subcarrier-by-subcarrier basis). In practice, sampling $r(t; \mathbf{c}_N)$ in (22) at the instant $t_{\tilde{n}} \triangleq \tilde{n} T_s$ yields

$$r_{\tilde{n}} \triangleq r(t_{\tilde{n}}; \mathbf{c}_N) = \frac{1}{\sqrt{N}} \sum_{n=-N_\alpha}^{N_\alpha} c_{R_N[n]} H_{R_N[n]} \exp\left(j2\pi \frac{\tilde{n}}{N} n\right), \tag{24}$$

with $\tilde{n} = 0, 1, ..., N-1$. The last equation can be easily written in vector form as

$$\mathbf{r}_N \triangleq [r_0, r_1, ..., r_{N-1}]^T = \mathbf{\Xi}_N^H(\mathbf{c}_N \odot \mathbf{H}), \tag{25}$$

where $\mathbf{H} \triangleq [H_0, H_1, ..., H_{N-1}]^T$. Performing an order N DFT of the N-dimensional vector $\mathbf{r}_N$ produces the N-dimensional vector

$$\mathbf{R}_N = \mathbf{\Xi}_N \mathbf{\Xi}_N^H(\mathbf{c}_N \odot \mathbf{H}) = \mathbf{c}_N \odot \mathbf{H}, \tag{26}$$

---

[3]The adoption of this filter follows from the model (3), that represents the complex envelope of an OFDM signal as the output signal of baseband pulse amplitude modulator.

whose nth element is

$$R_n = \frac{1}{N} c_n H_n \qquad (27)$$

for $0 \leq n \leq N_\alpha$ and $N - N_\alpha \leq n \leq N - 1$ (the remaining N_{sc} elements of $\mathbf{R}_N$ are irrelevant since, being associated with the SCs, are discarded). Note that the simplicity and the elegance of the model (27) follows from the *orthogonality* of the complex exponentials appearing in the RHS of (24). Moreover, from (27) it is easily inferred that c_n can be detected on the basis of R_n after compensating for the complex channel gain H_n. This elegant result has been obtained under the assumption that the complex envelope of the transmitted signal is expressed by (3), since this allows, under certain assumptions, to put it in the multicarrier form expressed by (19); this, in turn, leads easily to (22). Unluckily, all these signals have an infinite duration, so that, seemingly, an unlimited time interval is required for the transmission of a symbol vector of limited size. In practice, if the temporal supports of $p(t)$ and $h(t)$ are limited and, in particular, are the intervals $[0, L_p T_s]$ and $[0, L_h T_s]$ (where L_p and L_h are integer parameters), respectively, and if the integer parameter $N_{cp}^{(\text{TD})}$, representing the size of the CP, is not smaller than[4] $(2L_{\text{p}} + L_{\text{h}})$, it can be shown that (24) still holds in the interval $(0, NT_s)$ provided that (3) is replaced by its time limited counterpart

$$s(t; \mathbf{c}_N) = \sum_{k=-N_{cp}^{(\text{TD})}}^{N-1} x_k\, p(t - kT_s). \qquad (28)$$

Finally, it is useful to note that the interval devoted to the transmission of the CP can be also considered as a *guard interval* for avoiding the inference between consecutive OFDM symbols (i.e., the so called *inter-block interference*, IBI). Moreover, if the duration of the CP exceeds its minimum value, the performance of the considered communication system is not affected by a limited sampling offset. In fact, such an offset, that results in a phase rotation of all channel symbols, is compensated for through FD equalization.

B. Signal Models in a DOFDM-Based Communication System

In this subsection we focus on the derivation of various signal models for a communication system employing the DOFDM modulation; our approach parallels that provided for OFDM in the previous subsection and relies on the use of the duality principle; this means, for instance, that any DFT is replaced by an IDFT (and viceversa) and that TD signal models are replaced by the corresponding FD counterparts (and viceversa).

In the following, we take into consideration the transmission of a digital message represented by the M-dimensional vector $\mathbf{c}_M \triangleq [c_0, c_1, ..., c_{M-1}]^T$; we assume that each of its elements are *channel symbols* belonging to an $M_c$ary constellation and that M is even. The vector $\mathbf{c}_M$ undergoes an order M DFT (see (10)) at the TX side. This produces the M-dimensional vector

$$\mathbf{y}_M = \text{DFT}_M[\mathbf{c}_M] = \mathbf{\Xi}_M \mathbf{c}_M, \qquad (29)$$

which is periodically extended to generate the sequence $\{y_k\}$ having period M. In other words, the kth element of this sequence is expressed by

$$y_k = y_{R_M[k]} \qquad (30)$$

for any $k \notin \{0, 1, ..., M - 1\}$. This sequence is conveyed by the complex signal $s_D(t; \mathbf{c}_M)$, characterized by the *periodic spectrum*

$$S_D(f; \mathbf{c}_M) = \sum_{k=-\infty}^{+\infty} y_k P(f - k\Delta_f), \qquad (31)$$

that represents the dual of $s(t; \mathbf{c}_N)$ (3); here, $P(f)$ is the FCT of the pulse $p(t)$ employed in the generation of the modulated signal (further details about the properties of this pulse are provided below). Since the period of $S_D(f; \mathbf{c}_M)$ in (31) is equal to $B \triangleq M\Delta_f$, this spectrum can be represented through its Fourier series as

$$S_D(f; \mathbf{c}_M) = \sum_{q=-\infty}^{+\infty} s_q^{(\text{FD})}(\mathbf{c}_M) \exp(-j2\pi f t_q), \qquad (32)$$

---

[4]This means that the duration of the CP must not be shorter than the *overall memory* of the communication channel, provided that channel filtering also accounts for TX and RX filtering [6, Sec. 3.5.3]. Note that the duration of $p(t)$ plays an important role in determining the value of $N_{cp}^{(\text{TD})}$.

where $t_q \triangleq q/B = q/(M\Delta_f)$ and

$$s_q^{(\text{FD})}(\mathbf{c}_M) \triangleq \frac{1}{B} \int_{-M\Delta_f/2}^{M\Delta_f/2} S_D(f; \mathbf{c}_M) \exp(j2\pi f t_q)\, df \tag{33}$$

is the qth Fourier coefficient of $S_D(f; \mathbf{c}_M)$. Substituting the RHS of (31) in that of (33) and exploiting the periodicity of the sequence $\{y_k\}$ produces, after some manipulation,

$$s_q^{(\text{FD})}(\mathbf{c}_M) = \frac{1}{\sqrt{M}\Delta_f} p_q\, c_{R_M[q]}, \tag{34}$$

where

$$p_q \triangleq p(t_q) = p\left(\frac{q}{B}\right) = p\left(\frac{q}{M\Delta_f}\right). \tag{35}$$

Then, substituting the RHS of (34) in that of (32) yields

$$S_D(f; \mathbf{c}_M) = \frac{1}{\sqrt{M}\Delta_f} \sum_{q=-\infty}^{+\infty} p_q\, c_{R_M[q]} \exp(-j2\pi f t_q). \tag{36}$$

The last equation can be further simplified following the same approach as that illustrated for (14); for this reason, the index q is replaced by the couple (m, k) such that $q = m + kM$, with $m = 0, 1, ..., M-1$ and k arbitrary integer. This allows us to rewrite (36) as

$$S_D(f; \mathbf{c}_M) = \frac{1}{\sqrt{M}\Delta_f} \sum_{m=0}^{M-1} c_m G_m(f), \tag{37}$$

where

$$G_m(f) \triangleq \sum_{k=-\infty}^{+\infty} p_{m+kM} \exp(-j2\pi t_{m+kM} f). \tag{38}$$

Based on similar considerations as those illustrated for (15) and (16), we require $G_m(f)$ to consist of a single complex exponential, i.e., that, for any m, only a single term survives in the sum appearing in the RHS of (38). From (38) it is easily inferred that this result is achieved if $p(t)$ is *time-limited* and, in particular, if its duration does not exceed $1/\Delta_f$. Note that, when this occurs, $S_D(f; \mathbf{c}_M)$ consists of the superposition of M complex exponentials that are *orthogonal* in the frequency range $[-B/2, B/2]$ (i.e., over a single period of this spectrum). In the following, we assume that: 1) the support of $p(t)$ is contained in the interval $[-1/(2\Delta_f), 1/(2\Delta_f)]$ and $p_q = \sqrt{\Delta_f}$ for $q = -N_\beta, -N_\beta + 1, ..., -1, 0, 1, ..., N_\beta$, where N_β is a positive integer depending on the pulse shape and such that $N_u = (2N_\beta + 1) < M$; 2) $N_{sc} \triangleq M - N_u$ consecutive elements of $\mathbf{c}_M$ (and, in particular, the elements whose index runs from N_β to $M - N_\beta - 1$) are set to zero. Under these assumptions (37) becomes

$$S_D(f; \mathbf{c}_M) = \frac{1}{\sqrt{M}\Delta_f} \sum_{m=-N_\beta}^{N_\beta} c_{R_M[m]} \exp\left(-j2\pi f t_m\right), \tag{39}$$

so that it takes the form described above. This representation of $S_D(f; \mathbf{c}_M)$ holds in a single period (say, in the interval $\mathcal{I}_f \triangleq (-B/2, B/2)$) if $p(t)$ is bandlimited (with bandwidth B_p). In this case, the sum appearing in the RHS of (31) can be properly truncated to limit the number of its terms; this leads to the new spectrum[5]

$$Y_D(f; \mathbf{c}_M) = \sum_{k=-(M/2+N_{cp}^{(\text{FD})})}^{M/2-1+N_{cpo}^{(\text{FD})}} y_k P\left(f - k\Delta_f\right), \tag{40}$$

where the integer parameters $N_{cp}^{(\text{FD})}$ and $N_{cpo}^{(\text{FD})}$ denote the size of the CP and that of the *cyclic postfix* (CPO), respectively. Similarly as OFDM, the use of a CP and a CPO is needed to guarantee that, over the considered frequency range, the observed spectrum looks periodic, i.e., that it has a *quasi-periodic structure* (details about the

---

[5]Note that a larger value of B_p results in a longer prefix and in a longer postfix; i.e., requires increasing the values of $N_{cp}^{(\text{FD})}$ and $N_{cpo}^{(\text{FD})}$.

selection of $N_{cp}^{(\text{FD})}$ and $N_{cpo}^{(\text{FD})}$ are provided below). Given the spectrum in (40), the complex envelope $y_D(t; \mathbf{c}_M)$ of the transmitted signal is expressed by its *inverse* FCT (IFCT), that is

$$y_D(t; \mathbf{c}_M) \triangleq \text{IFCT}\Big[Y_D(f; \mathbf{c}_M)\Big] = p(t) \sum_{k=-(M/2+N_{cp}^{(\text{FD})})}^{M/2-1+N_{cpo}^{(\text{FD})}} y_k \exp(j2\pi k \Delta_f t). \tag{41}$$

This means that the complex envelope of the DOFDM modulation is the superposition of multiple complex exponentials windowed by $p(t)$. Note that this signal model is structurally similar to the model (19) developed for OFDM, but is characterized by a subcarrier spacing equal to Δ_f. However, in the case of DOFDM, the set of channel symbols $\{c_{R_N[n]}\}$ is replaced by the set of their DFT coefficients (namely, by the set $\{y_k\}$), and the presence of both a CP and a CPO is required; moreover, the role of $p(t)$, acting as a TD window, is also clear.

Let us consider now the transmission of $y_D(t; \mathbf{c}_M)$ in (41) on the dual of a frequency selective channel, i.e., on a *time selective channel*. This channel introduces the multiplicative distortion (see [6, eq. (2.134)])

$$a(t) \triangleq \sum_{l=0}^{L-1} a_l \exp(j2\pi\nu_l t) \tag{42}$$

in the TD; here, a_l and ν_l represent the lth complex gain and the corresponding Doppler shift (with $l = 0, 1, ..., L-1$), respectively, and L is the overall number of Doppler shifts characterizing the communication channel. Let also

$$B_D \triangleq 2 \max_l |\nu_l| \tag{43}$$

denote the *Doppler bandwidth* of the communication channel. The spectrum of the channel response $z_D(t; \mathbf{c}_M)$ to $y_D(t; \mathbf{c}_M)$ in (41) can be evaluated as

$$Z_D(f; \mathbf{c}_M) = Y_D(f; \mathbf{c}_M) * A(f) = \sum_{k=-(M/2+N_{cp}^{(\text{FD})})}^{M/2-1+N_{cpo}^{(\text{FD})}} y_k P_{\text{a}}(f - k\Delta_f), \tag{44}$$

where $A(f)$ denotes the FCT of $a(t)$ (42) and

$$P_{\text{a}}(f) = P(f) * A(f) \tag{45}$$

represents the FCT of the pulse $p(t)$ distorted by the communication channel, i.e., of the signal[6]

$$p_{\text{a}}(t) \triangleq \text{IFCT}[P_{\text{a}}(f)] = p(t)\, a(t). \tag{46}$$

Note that, if (42) holds, we have that

$$P_{\text{a}}(f) = \sum_{l=0}^{L-1} a_l P(f - \nu_l). \tag{47}$$

At the RX side, matched filtering is executed in the FD; this means that the signal $Z_D(f; \mathbf{c}_M)$, in (44), is applied to a filter matched to $P(f)$, i.e., to a filter whose impulse response is $P^*(-f)$. The filter output is the spectrum

$$R_D(f; \mathbf{c}_M) = Z_D(f; \mathbf{c}_M) * P^*(-f). \tag{48}$$

The spectrum $Z_D(f; \mathbf{c}_M)$, in (44), looks periodic over the interval $\mathcal{I}_f$ and, consequently, can be represented as (see (39))

$$Z_D(f; \mathbf{c}_M) = \frac{1}{\sqrt{M\Delta_f}} \sum_{m=-N_\beta}^{N_\beta} c_{R_M[m]}\, a_{R_M[m]} \cdot \exp(-j2\pi f t_m) \tag{49}$$

in that interval; here,

$$a_m \triangleq a(t_m) = a(m/B) = a(m/(M\Delta_f)) \tag{50}$$

---

[6]Note that the bandwidth of $p_{\text{a}}(t)$ is equal to $B_{\text{p}} + B_D$. Therefore, it is larger than that of $p(t)$ because of the spectral broadening due to the Doppler phenomenon.

for any m. Then, substituting the RHS of (49) in that of (48) yields

$$R_D(f; \mathbf{c}_M) = \frac{1}{\sqrt{M\Delta_f}} \sum_{m=-N_\beta}^{N_\beta} c_{R_M[m]} a_{R_M[m]} \cdot \exp(-j2\pi f t_m) p^*(t_m) \tag{51}$$

Sampling $R_D(f; \mathbf{c}_M)$ at the frequency $\bar{f}_k = k\Delta_f$, with $k = -M/2, -M/2+1, ..., -1, 0, 1, ..., M/2-1$, gives

$$R_{D,k} \triangleq R_D(\bar{f}_k; \mathbf{c}_M) = \frac{1}{\sqrt{M}} \sum_{m=-N_\beta}^{N_\beta} c_{R_M[m]} a_{R_M[m]} \cdot \exp\left(-j2\pi k \frac{m}{M}\right). \tag{52}$$

The last equation can be easily written in vector form as

$$\mathbf{R}_{D,M} \triangleq [R_{D,0}, R_{D,1}, ..., R_{D,M-1}]^T = \mathbf{\Xi}_M(\mathbf{c}_M \odot \mathbf{a}), \tag{53}$$

where $\mathbf{a} \triangleq [a_0, a_1, ..., a_{M-1}]^T$. Performing an order M IDFT of the vector $\mathbf{R}_{D,M}$ produces the M-dimensional vector

$$\mathbf{r}_{D,M} = \mathbf{\Xi}_M^H \mathbf{\Xi}_M(\mathbf{c}_M \odot \mathbf{a}) = \mathbf{c}_M \odot \mathbf{a}, \tag{54}$$

whose mth element is given by

$$r_{D,m} = \frac{1}{M} c_m a_m, \tag{55}$$

for $0 \leq n \leq N_\beta$ and $M - N_\beta \leq n \leq M - 1$ (the remaining N_{sc} elements of $\mathbf{r}_{D,M}$ are irrelevant since, being associated with the suppressed carriers, are discarded). The last result represents the TD counterpart of the FD formula (27). For this reason, symbol detection can be carried out in a similar way after equalizing the communication channel; this task, in turn, requires estimating the complex samples $\{a_m\}$, i.e., multiple samples of the multiplicative distortion introduced by the communication channel.

Finally, it is important to point out that:

1) A TD RC pulse could be adopted for $p(t)$. The value of N_β for this pulse depends on the value of the RC roll-off (similarly to OFDM, a smaller roll-off results in a wider flat top of the pulse and, consequently, in a larger N_β).

2) The values of both the CP $N_{cp}^{(\text{FD})}$ and the CPO $N_{cpo}^{(\text{FD})}$ should not be smaller than $\lceil (2B_{\text{p}} + B_D)/(2\Delta_f) \rceil$ in order to ensure the property of *spectral cyclicity* in the frequency range of interest $(-M\Delta_f/2, M\Delta_f/2)$.

3) The TD counterpart of (48) is

$$r_D(t; \mathbf{c}_M) = z_D(t; \mathbf{c}_M) p^*(t), \tag{56}$$

where $r_D(t; \mathbf{c}_M)$ and $z_D(t; \mathbf{c}_M)$ represent the IFCT of $R_D(f; \mathbf{c}_M)$ and $Z_D(f; \mathbf{c}_M)$, respectively. This means that, in practice, at the RX side, the received signal $r_D(t; \mathbf{c}_M)$ undergoes windowing (represented by a multiplication by $p^*(t)$) and, then, spectral analysis for the evaluation of the samples $\{R_D(\bar{f}_k; \mathbf{c}_M)\}$. The last task can be executed by sampling $r_D(t; \mathbf{c}_M)$ at a proper rate and accomplishing a DFT on the resulting sample sequence.

C. Signal Models in an OTFS-Based Communication System

In this subsection we first show how the mathematical results illustrated in the previous two subsections can be exploited to: 1) develop various models for the complex envelope of an OTFS signal incorporating a DCP; 2) derive the corresponding received signal model in the presence of both an ideal communication channel and a doubly selective fading channel. Then, we analyze the implications of selecting a specific pulse shape in the OTFS signal model. Our approach is inspired by the basic principles illustrated for OFDM and its dual, and aims at developing a digital modulation format whose detection and equalization can be implemented at a reasonable complexity in the presence of a doubly selective communication channel.

1) Transmitted signal model: In the following, we take into consideration the transmission of the $M \times N$ matrix[7] $\mathbf{C} \triangleq [c_{m,n}]$ (with $m = 0, 1, ..., M-1$ and $n = 0, 1, ..., N-1$), collecting MN channel symbols, each of which belongs to an $M_c$ary constellation; this matrix represents a single OTFS *symbol*. Let us assume that the matrix $\mathbf{C}$ undergoes a one-to-one transformation $\mathbf{g} : \mathbb{C}^{M \times N} \to \mathbb{C}^{M \times N}$, generating the transformed symbol matrix

$$\mathbf{X} \triangleq [x_{m,n}] = \mathbf{g}(\mathbf{C}), \tag{57}$$

having the same size as $\mathbf{C}$. The matrix $\mathbf{X}$ is periodically extended along both its dimensions to generate the 2D periodic sequence

$$x_{k,l} = x_{R_M[k], R_N[l]}, \tag{58}$$

for any value of the couple (k, l) not belonging to the set of indices of the elements of $\mathbf{X}$ (57). The matrix $\mathbf{X}$ is transmitted by generating a modulated signal that exhibits the property of *cyclicity in both the TD and the FD*. As shown in Subsections II-A and II-B, cyclicity in the TD over an interval lasting NT_s s and in the FD over the frequency range $(-M\Delta_f/2, M\Delta_f/2)$ can be guaranteed by generating the complex envelope (see (28))

$$s(t; \mathbf{C}) \triangleq \sum_{l=-N_{cp}^{(\text{TD})}}^{N-1} s_l^{(\text{FD})} \left(t - lT_s; \mathbf{C} \right), \tag{59}$$

with (see (41))

$$s_l^{(\text{FD})} \left(t; \mathbf{C} \right) \triangleq p(t) \sum_{k=-(M/2+N_{cp}^{(\text{FD})})}^{M/2-1+N_{cpo}^{(\text{FD})}} x_{k,l} \exp\left(j2\pi k \Delta_f t \right); \tag{60}$$

here, $p(t)$ is a bandlimited pulse (whose temporal support is the interval $[0, L_p T_s]$, L_p being an integer parameter), T_s is the symbol interval, Δ_f is a frequency spacing, and the integer parameters $N_{cp}^{(\text{TD})}$, $N_{cp}^{(\text{FD})}$ and $N_{cpo}^{(\text{FD})}$ have the same meaning and scope as that illustrated for the corresponding parameters which have been defined in our description of OFDM and DOFDM, respectively. Note that the DCP insertion entails the transmission of

$$N_{cp} \triangleq N_{cp}^{(\text{TD})} M + (N + N_{cp}^{(\text{TD})})(N_{cp}^{(\text{FD})} + N_{cpo}^{(\text{FD})}) \tag{61}$$

additional channel symbols, so that

$$\Lambda_{cp} \triangleq \frac{N_{cp}}{MN + N_{cp}} \tag{62}$$

represents the fraction of channel symbols assigned to the TD prefix and to the FD prefix & postfix. Substituting the RHS of (60) in that of (59) yields the signal model

$$s(t; \mathbf{C}) = \sum_{l=-N_{cp}^{(\text{TD})}}^{N-1} \sum_{k=-(M/2+N_{cp}^{(\text{FD})})}^{M/2-1+N_{cpo}^{(\text{FD})}} x_{k,l} p\left(t - lT_s \right) \cdot \exp\left(j2\pi k \Delta_f \left(t - lT_s \right) \right), \tag{63}$$

that has the same structure as [4, Sec. II-A, eq. (5)], but, unlike that, includes a *double cyclic extension*. Note also that (63) can be easily rewritten as

$$s(t; \mathbf{C}) = \sum_{k=-(M/2+N_{cp}^{(\text{FD})})}^{M/2-1+N_{cpo}^{(\text{FD})}} s_k^{(\text{TD})}(t; \mathbf{C}), \tag{64}$$

where

$$s_k^{(\text{TD})}(t; \mathbf{C}) \triangleq \sum_{l=-N_{cp}^{(\text{TD})}}^{N-1} x_{k,l} \, p(t - lT_s) \exp\left(j2\pi k \Delta_f (t - lT_s) \right), \tag{65}$$

---

[7]The values of the parameters M and N are assumed to be even in the following.

and that the last signal can be interpreted as a frequency shifted version of an OFDM signal (with a frequency shift equal to $k\Delta_f$; see (28)); consequently, $s(t; \mathbf{C})$ (64) can be seen as the superposition of multiple (namely, $M + N_{cp}^{(\mathrm{FD})} + N_{cpo}^{(\mathrm{FD})}$) OFDM signals, characterized by distinct central frequencies. Let us select now[8]

$$\Delta_f = 1/T_s, \tag{66}$$

so that $s_k^{(\mathrm{TD})}(t; \mathbf{C})$ (65) looks periodic, with period

$$T = NT_s, \tag{67}$$

in the interval $[0, T]$. Therefore, in that interval, it can be represented through the FS (see (4) and (5))

$$s_k^{(\mathrm{TD})}(t; \mathbf{C}) = \sum_{q=-\infty}^{+\infty} S_{k,q}^{(\mathrm{TD})}(\mathbf{C}) \exp\left(j2\pi q \frac{t}{T}\right), \tag{68}$$

where

$$S_{k,q}^{(\mathrm{TD})}(\mathbf{C}) \triangleq \frac{1}{T} \int_0^T s_k^{(\mathrm{TD})}(t; \mathbf{C}) \exp\left(-j2\pi q \frac{t}{T}\right) dt \tag{69}$$

is the qth Fourier coefficient. The coefficient $S_{k,q}^{(\mathrm{TD})}(\mathbf{C})$ (69) can be evaluated by: 1) replacing the extremes $(-N_{cp}^{(\mathrm{TD})})$ and $(N-1)$ of the summation in (68) with $-\infty$ and $+\infty$, respectively[9]; 2) substituting the RHS of the resulting formula in that of (69); 3) replacing the index l with the couple $(\tilde{l}, u)$ such that $l = \tilde{l} + uN$, with $\tilde{l} = 0, 1, ..., N-1$ and u arbitrary integer; 4) exploiting the periodicity, with period N, of the sequence $\{x_{k,l}\}$ in the index l (see (58)). This yields, after some manipulation[10],

$$S_{k,q}^{(\mathrm{TD})}(\mathbf{C}) = \frac{1}{\sqrt{N}T_s} X_{k,q} P\left(\frac{q - kN}{T}\right), \tag{70}$$

where $P(f)$ is the FCT of $p(t)$ and

$$X_{k,q} \triangleq \frac{1}{\sqrt{N}} \sum_{n=0}^{N-1} x_{k,n} \exp\left(-j2\pi \frac{n}{N} q\right) \tag{71}$$

represents the qth element of the order N DFT of the sequence $\{x_{k,n}\}$ evaluated with respect to the index n.

The mathematical results developed until now (and, in particular, the FS representation (68)) allow us to analyze easily what happens at the RX side when $s(t; \mathbf{C})$ (63) is transmitted on an *ideal communication channel*, i.e., on a channel that does not introduce distortion and noise (channel delay is also neglected for simplicity). The study of this scenario, which is described in the following paragraph, allows us to: 1) discover the nature of the transformation $\mathbf{g}(\cdot)$ to be adopted in (57); 2) assess the impact of TX and RX filtering.

2) Received signal model in the presence of an ideal communication channel: Following [19], [20], we assume that the first stage in the baseband model of the receiver for the modulation format described in the previous paragraph is a *filter bank*[11], consisting of M distinct *matched filters*. The frequency response and the impulse response of the $\tilde{k}$th filter (matched to $p(t) \exp(j2\pi k\Delta_f t)$) are

$$\Phi_{\tilde{k}}(f) = P^*\left(f - \tilde{k}\Delta_f\right) = P^*\left(f - \tilde{k}N/T\right) \tag{72}$$

and

$$\phi_{\tilde{k}}(t) = p^*(-t) \exp\left(j2\pi \tilde{k}t/T_s\right), \tag{73}$$

respectively, with $\tilde{k} = -M/2, -M/2+1, ..., M/2-1$. Based on the signal decomposition (64), the overall response of this filter to the signal $s(t; \mathbf{C})$ (63), can be computed by first evaluating its response to $s_k^{(\mathrm{TD})}(t; \mathbf{C})$ (65) and then

[8]This assumption is commonly made in the technical literature (e.g., see [13]); this corresponds to selecting the subcarrier spacing of OFDM equal to Δ_f/N, i.e., N times smaller than that characterizing DOFDM (see our comments above (20) and those following (41)).

[9]Note that this does not have any impact on the representation of $s_k^{(\mathrm{TD})}(t; \mathbf{C})$ (65) over the limited interval $[0, T]$.

[10]The derivation of the following result is similar to that illustrated for (6) (obtained from (5)); further details can be found in Appendix A.

[11]This choice is optimal in the maximum likelihood sense in this case, but is sub-optimal in the case of a multipath fading channel.

summing over k. Based on the FS representation (68) of $s_k^{(\text{TD})}(t; \mathbf{C})$ and (72), the last response can be expressed as

$$r_{k,\tilde{k}}(t; \mathbf{C}) = \frac{1}{\sqrt{N}} \sum_{q=-\infty}^{+\infty} X_{k,q} \, G_{k,\tilde{k},q} \exp\left(j2\pi q \frac{t}{T}\right), \tag{74}$$

in the interval[12] $[0, T]$; here,

$$G_{k,\tilde{k},q} \triangleq \frac{1}{T_s} P\left(\frac{q - kN}{T}\right) P^*\left(\frac{q - \tilde{k}N}{T}\right) \tag{75}$$

for any k, $\tilde{k}$ and q. The output of the $\tilde{k}$th matched filter (with $\tilde{k} = -M/2, -M/2 + 1, ..., M/2 - 1$) is sampled at the instant $t_{\tilde{n}} = \tilde{n} T_s$, with $\tilde{n} = 0, 1, ..., N - 1$. Sampling $r_{k,\tilde{k}}(t; \mathbf{C})$ (74) at that instant produces[13]

$$r_k[\tilde{k}, \tilde{n}] \triangleq r_{k,\tilde{k}}(t_{\tilde{n}}; \mathbf{C}) = \frac{1}{\sqrt{N}} \sum_{q=-\infty}^{+\infty} X_{k,q} \, G_{k,\tilde{k},q} \exp\left(j2\pi \frac{q}{N} \tilde{n}\right). \tag{76}$$

The last expression can be easily rewritten by: 1) replacing the index q with the couple $(\tilde{q}, u)$, with $\tilde{q} = 0, 1, ..., N-1$ and u arbitrary integer; 2) replacing $\tilde{q}$ with q; 3) exploiting the periodicity of the sequence $\{X_{k,q}\}$ in q (with period N). This yields

$$r_k[\tilde{k}, \tilde{n}] = \frac{1}{\sqrt{N}} \sum_{q=0}^{N-1} X_{k,q} \, \hat{G}_{\tilde{k}-k,q} \exp\left(j2\pi \frac{q}{N} \tilde{n}\right), \tag{77}$$

where

$$\hat{G}_{x,q} \triangleq \frac{1}{T_s} \sum_{u=-\infty}^{+\infty} P\left(\frac{q + (u + x)N}{T}\right) P^*\left(\frac{q + uN}{T}\right) \tag{78}$$

for any x. Given (77), the output $r[\tilde{k}, \tilde{n}]$ of the $\tilde{k}$th matched filter at the instant $t_{\tilde{n}} = \tilde{n} T_s$ can be evaluated as

$$r[\tilde{k}, \tilde{n}] = \sum_{k=-\infty}^{+\infty} r_k[\tilde{k}, \tilde{n}]. \tag{79}$$

Then, substituting the RHS of (77) in that of the last equation gives, after some manipulations (further details are provided in Appendix B),

$$r[\tilde{k}, \tilde{n}] = \frac{1}{\sqrt{MN}} \sum_{p=0}^{M-1} \sum_{q=0}^{N-1} \bar{X}_{p,q} \, \bar{g}_{p,q} \cdot \exp\left(-j2\pi \left(\frac{p}{M} \tilde{k} - \frac{q}{N} \tilde{n}\right)\right), \tag{80}$$

where

$$\bar{X}_{p,q} \triangleq \frac{1}{\sqrt{M}} \sum_{m=0}^{M-1} X_{m,q} \exp\left(j2\pi \frac{p}{M} m\right) \tag{81}$$

is the pth element of the order M IDFT of the sequence $\{X_{m,q}\}$ in the index m and

$$\bar{g}_{p,q} \triangleq \sum_{u=-\infty}^{+\infty} \hat{G}_{u,q} \exp\left(j2\pi \frac{p}{M} u\right) \tag{82}$$

represents the *frequency response*, evaluated at the normalized frequency (p/M), of the digital filter characterized by the impulse response $\{\hat{G}_{u,\cdot}\}$ (further details can be found in Appendix B).

Equation (80) leads to the conclusion that the 2D sequence $\{r[\tilde{k}, \tilde{n}]\}$ consists of the superposition of MN distinct complex exponentials and that the complex gain associated with the couple of indices (p, q) is given by the product between $\bar{X}_{p,q}$ (conveying the transmitted information) and $\bar{g}_{p,q}$ (depending on TX and RX filtering only). Based on the last results, we can: 1) select properly the transformation $\mathbf{g}(\cdot)$; 2) assess the impact of the pulse $p(t)$ on the

---

[12]Despite RX filtering, this interval remains the same as that in which (68) holds, thanks to the fact that the employed matched filters are assumed not to be causal for simplicity (see (73)).

[13]In the following, the dependence on $\mathbf{C}$ is omitted to ease notation.

structure of the received samples. In the remaining part of this paragraph, we concentrate on the first issue only (a detailed discussion on the second one can be found in Paragraph II-C.4). As far as $\mathbf{g}(\cdot)$ is concerned, substituting the RHS of (71) in that of (81) gives

$$\bar{X}_{p,q} \triangleq \frac{1}{\sqrt{MN}} \sum_{m=0}^{M-1} \sum_{n=0}^{N-1} x_{m,n} \exp\left(j2\pi\left(\frac{m}{M}p - \frac{n}{N}q\right)\right), \tag{83}$$

that can be interpreted as the coefficient (p,q) of the order (M,N) *Symplectic Discrete Fourier Transform* (SDFT) of the $M \times N$ complex matrix $\mathbf{X}$ [12], [13]. Note that (83) can be rewritten in matrix form as

$$\bar{\mathbf{X}} = \mathrm{SDFT}_{M,N}[\mathbf{X}] \triangleq \mathbf{\Xi}_M^H \, \mathbf{X} \, \mathbf{\Xi}_N, \tag{84}$$

where $\bar{\mathbf{X}} \triangleq [\bar{X}_{p,q}]$ is an $M \times N$ complex matrix. This suggests to select an order (M,N) *inverse* SDFT (ISDFT) for the transformation $\mathbf{g}(\cdot)$ appearing in the RHS of (57), so that

$$\mathbf{X} = \mathrm{ISDFT}_{M,N}[\mathbf{C}] \triangleq \mathbf{\Xi}_M \, \mathbf{C} \, \mathbf{\Xi}_N^H. \tag{85}$$

In fact, (84) implies that

$$\bar{\mathbf{X}} = \mathbf{\Xi}_M^H \, \mathbf{\Xi}_M \, \mathbf{C} \, \mathbf{\Xi}_N^H \, \mathbf{\Xi}_N = \mathbf{C} \tag{86}$$

and, consequently, that

$$\bar{X}_{p,q} = c_{R_M[p], R_N[q]}, \tag{87}$$

for any p and q, and (see (80))

$$r[\tilde{k}, \tilde{n}] = \frac{1}{\sqrt{MN}} \sum_{p=0}^{M-1} \sum_{q=0}^{N-1} c_{p,q} \, \bar{g}_{p,q} \cdot \exp\left(-j2\pi\left(\frac{p}{M}\tilde{k} - \frac{q}{N}\tilde{n}\right)\right). \tag{88}$$

The last result can be easily rewritten in matrix form as

$$\mathbf{r}(\mathbf{C}) = \mathbf{\Xi}_M (\mathbf{C} \odot \bar{\mathbf{G}}) \mathbf{\Xi}_N^H, \tag{89}$$

where $\mathbf{r}(\mathbf{C}) \triangleq [r[\tilde{k}, \tilde{n}]]$ and $\bar{\mathbf{G}} \triangleq [\bar{g}_{p,q}]$ are $M \times N$ matrices collecting the received signal samples acquired at the output of whole filter bank over our observation interval and the complex gains $\{\bar{g}_{p,q}\}$ (evaluated on the basis of (82)). Moreover, based on (89), a simple detection method, conceptually similar to those illustrated for OFDM and DOFDM, can be easily developed. In fact, performing an order (M,N) SDFT on $\mathbf{r}(\mathbf{C})$ (89) produces the $M \times N$ complex matrix

$$\mathbf{Y}(\mathbf{C}) \triangleq \mathrm{SDFT}_{M,N}[\mathbf{r}(\mathbf{C})] = \mathbf{C} \odot \bar{\mathbf{G}}, \tag{90}$$

whose element (m,n) is

$$Y[m,n] = \frac{1}{MN} c_{m,n} \bar{g}_{m,n}, \tag{91}$$

with $m = 0, 1, ..., M-1$ and $n = 0, 1, ..., N-1$. Then, for any m and n, the channel symbol $c_{m,n}$ has to be be detected on the basis of $Y[m,n]$ only, after compensating for the complex gain $\bar{g}_{m,n}$.

It is important to point out that:

1) Equations (85) and (87) entail that

$$x_{m,n} \triangleq \frac{1}{\sqrt{MN}} \sum_{p=0}^{M-1} \sum_{q=0}^{N-1} c_{p,q} \exp\left(-j2\pi\left(\frac{p}{M}m - \frac{q}{N}n\right)\right), \tag{92}$$

with $m = 0, 1, ..., M-1$ and $n = 0, 1, ..., N-1$.

2) The mathematical result expressed by (91) can be seen as a generalization of (27) and (55), that have been derived for OFDM and DOFDM, respectively. Note that the absence of any form of ISI affecting $Y[m,n]$ (91) is made possible by the use of a DCP[14]. In fact, this property would disappear if the TD CP and/or the FD CP &

---

[14]In the absence of a DCP, (77) and (158) (see Appendix B), and, consequently, (80), would not hold. This would result in the presence of a 2D ISI term in the RHS of (91).

CPO were removed. Note also that, since the communication channel we are considering does not introduce any distortion, the coefficient $\bar{g}_{m,n}$ depends exclusively on the spectrum $P(f)$ (see (82) and (78)).

3) Ideally, the pulse $p(t)$ should be selected in a way that all the elements of the resulting gain matrix $\bar{\mathbf{G}}$ have similar amplitudes (see (90)); in fact, this would ensure that all the channel symbols are treated fairly, i.e., that the 2D complex exponentials conveying them exhibit similar strengths. It should be expected, however, that, similarly to what happens in the case of OFDM and DOFDM, since this condition cannot be met for all the elements of the matrix $\mathbf{C}$, even in an approximate fashion, a portion of such elements has to be suppressed (i.e., set to zero). These issues are discussed in detail in Paragraph II-C.4.

3) Received signal model in the presence of a doubly selective fading channel: Let us focus now on the reception on a multipath fading channel characterized by *channel impulse response*[15] (CIR)

$$h(t, \tau) = \sum_{l=0}^{L-1} \tilde{h}_l(t, \tau), \tag{93}$$

where

$$\tilde{h}_l(t, \tau) = a_l \exp(j2\pi\nu_l t)\delta(\tau - \tau_l) \tag{94}$$

represents the CIR component associated with the lth path, characterized by the delay τ_l and the Doppler shift ν_l, and L is the overall number of paths. In the following, we assume that the CIR components are organized according to increasing delays, so that τ_0 and τ_{L-1} represent the minimum and maximum delays, respectively. In the remaining part of this subsection, we derive a mathematical model for the $M \times N$ matrix $\mathbf{r}(\mathbf{C})$ collecting the samples acquired at the output of the above mentioned filter bank (see (89)) in the new scenario. Our analytical developments follow closely those illustrated above for an ideal communication channel. To begin, we evaluate the response

$$z_{k,l}(t; \mathbf{C}) \triangleq \int_{-\infty}^{+\infty} s_k^{(\mathrm{TD})}(\tau; \mathbf{C})\tilde{h}_l(\tau, t - \tau) \, d\tau \tag{95}$$

of the lth CIR contribution (namely, $\tilde{h}_l(t, \tau)$ (94)) to $s_k^{(\mathrm{TD})}(t; \mathbf{C})$ (65). Once again, in doing so, the FS representation (68) of $s_k^{(\mathrm{TD})}(t; \mathbf{C})$ is exploited; based on this, it is easy to prove that

$$z_{k,l}(t; \mathbf{C}) = \tilde{a}_l \sum_{q=-\infty}^{+\infty} Z_{k,q,l}(\mathbf{C}) \exp\left(j2\pi\left(\frac{q}{T} + \nu_l\right)t\right) \tag{96}$$

in the interval $[\tau_{L-1}, T + \tau_{L-1}]$; here,

$$Z_{k,q,l}(\mathbf{C}) \triangleq \frac{1}{\sqrt{N}T_s} X_{k,q} P\left(\frac{q - kN}{T}\right) \exp\left(-j2\pi q\frac{\tau_l}{T}\right) \tag{97}$$

and

$$\tilde{a}_l \triangleq a_l \exp\left(j2\pi\nu_l\tau_l\right). \tag{98}$$

Note that the difference between the coefficient (97) and its counterpart $S_{k,q}^{(\mathrm{TD})}(\mathbf{C})$ (70) obtained for an ideal channel is represented by a complex exponential, that accounts for the delay τ_l introduced by the lth path of the communication channel.

Given (96), the response

$$r_{k,\tilde{k},l}(t; \mathbf{C}) = z_{k,l}(t; \mathbf{C}) * \phi_{\tilde{k}}(t) \tag{99}$$

of the $\tilde{k}$th matched filter (see (72) and (73)) to $z_{k,l}(t; \mathbf{C})$ can be expressed as

$$r_{k,\tilde{k},l}(t; \mathbf{C}) = \tilde{a}_l \sum_{q=-\infty}^{+\infty} Z_{k,q,l}(\mathbf{C})P^*\left(\frac{q - \tilde{k}N}{T} + \nu_l\right) \cdot \exp\left(j2\pi\left(\frac{q}{T} + \nu_l\right)t\right). \tag{100}$$

---

[15]Channel sparsity is usually assumed in the OTFS literature (e.g., see [4], [12], [13], [21]). This assumption is not required in the following derivations.

Then, substituting the RHS of (97) in that of the last equation and sampling the resulting signal at the instant $t_{\tilde{n}} = \tau_{L-1} + \tilde{n}T_s$ produces

$$r_{k,l}[\tilde{k}, \tilde{n}] \triangleq r_{k,\tilde{k},l}(t_{\tilde{n}}; \mathbf{C}) = \frac{A_l}{\sqrt{N}} \exp(j2\pi\tilde{n}F_{\nu_l}) \cdot \sum_{q=-\infty}^{+\infty} X_{k,q} \, G_{k,\tilde{k},q,l} \exp\left(-j2\pi q \frac{F_{\tau_l}}{N}\right) \exp\left(j2\pi \frac{q}{N}\tilde{n}\right), \quad (101)$$

with $\tilde{n} = 0, 1, ..., N-1$; here,

$$G_{k,\tilde{k},q,l} \triangleq \frac{1}{T_s} P\left(\frac{q - kN}{T}\right) P^*\left(\frac{q - \tilde{k}N}{T} + \nu_l\right), \quad (102)$$

and

$$A_l \triangleq \tilde{a}_l \exp(j2\pi\nu_l\tau_{L-1}), \quad (103)$$

$$F_{\tau_l} \triangleq \frac{\tau_l - \tau_{L-1}}{T_s} \quad (104)$$

and

$$F_{\nu_l} \triangleq \nu_l T_s \quad (105)$$

denote a complex gain, the *normalized delay* and the *normalized Doppler shift* associated with the lth path, respectively. Given (101), the expression of the overall output of the $\tilde{k}$th RX filter due to the lth path and to all the components of $s(t; \mathbf{C})$ at the same sampling instant is evaluated by summing over k; this produces (further mathematical details are provided in Appendix C)

$$r_l[\tilde{k}, \tilde{n}] = \frac{A_l}{\sqrt{MN}} \exp\left(-j2\pi\tilde{k}F_{\tau_l}\right) \exp(j2\pi\tilde{n}F_{\nu_l}) \cdot \sum_{p=0}^{M-1}\sum_{q=0}^{N-1} \bar{X}_{p,q} \, \bar{g}_{p,q}(F_{\tau_l}, F_{\nu_l}) \exp\left(-j2\pi\left(\frac{p}{M}\tilde{k} - \frac{q}{N}\tilde{n}\right)\right), \quad (106)$$

where $\bar{X}_{p,q}$ is still expressed by (83), whereas

$$\bar{g}_{p,q}(F_{\tau_l}, F_{\nu_l}) \triangleq \sum_{u=-\infty}^{\infty} \hat{G}_{u,q}(F_{\tau_l}, F_{\nu_l}) \exp\left(j2\pi\frac{u}{M}p\right) \quad (107)$$

represents the counterpart of $\bar{g}_{p,q}$ (82). Note that (106) can be rewritten as

$$r_l[\tilde{k}, \tilde{n}] = h_l[\tilde{k}, \tilde{n}]T_l[\tilde{k}, \tilde{n}], \quad (108)$$

where

$$h_l[\tilde{k}, \tilde{n}] \triangleq A_l \exp\left(-j2\pi\tilde{k}F_{\tau_l}\right) \exp(j2\pi\tilde{n}F_{\nu_l}) \quad (109)$$

depends on the parameters of the lth path only, whereas

$$T_l[\tilde{k}, \tilde{n}] \triangleq \frac{1}{\sqrt{MN}} \sum_{p=0}^{M-1}\sum_{q=0}^{N-1} c_{p,q}\bar{g}_{p,q}(F_{\tau_l}, F_{\nu_l}) \cdot \exp\left(-j2\pi\left(\frac{p}{M}\tilde{k} - \frac{q}{N}\tilde{n}\right)\right) \quad (110)$$

depends on: 1) the channel symbols $\{c_{p,q}\}$; 2) the pulse shape, and the lth *normalized delay* and *Doppler shift* through $\bar{g}_{p,q}(F_{\tau_l}, F_{\nu_l})$.

Equation (106) describes the contribution given to the output of the $\tilde{k}$th RX filter by the lth path only. The contribution of all the paths can be accounted for by summing over the index l (see (93)); this produces (see (108))

$$r[\tilde{k}, \tilde{n}] \triangleq \sum_{l=0}^{L-1} r_l[\tilde{k}, \tilde{n}] = \sum_{l=0}^{L-1} h_l[\tilde{k}, \tilde{n}]T_l[\tilde{k}, \tilde{n}] \quad (111)$$

that, similarly as (80), expresses the $\tilde{n}$th sample taken at the output of the $\tilde{k}$th RX filter. The samples acquired at the output of the filter bank at all the considered sampling instants are collected in the $M \times N$ matrix $\mathbf{r}(\mathbf{C}) \triangleq [r[\tilde{k}, \tilde{n}]]$, that, similarly as the case of ideal channel, undergoes SDFT processing (see (90)); this yields

$$\mathbf{Y}(\mathbf{C}) \triangleq [Y[m, n]] = \text{SDFT}_{M,N}[\mathbf{r}(\mathbf{C})]. \quad (112)$$

It is easy to prove that the element (m, n) of $\mathbf{Y}(\mathbf{C})$ (112) is

$$Y[m,n] = \frac{1}{MN} \sum_{p=0}^{M-1} \sum_{q=0}^{N-1} c_{p,q} \left[\sum_{l=0}^{L-1} A_l \, \bar{g}_{p,q}(F_{\tau_l}, F_{\nu_l}) \cdot \Psi_M(m-p, -F_{\tau_l}) \Psi_N(n-q, F_{\nu_l}) \right], \tag{113}$$

where

$$\Psi_V(v, F) \triangleq \frac{\exp(j2\pi(v + FV)) - 1}{\exp\left(j2\pi\left(\frac{v+FV}{V}\right)\right) - 1} \tag{114}$$

and F is a normalized frequency belonging to the interval $[0, 1]$. Comparing (91) with (113) evidences that:

1) The presence of time dispersion (i.e., multipath) and frequency dispersion (i.e., Doppler) results in the presence of 2D ISI[16]. In fact, the RHS of (113) depends not only on $c_{m,n}$, but also on all the other channel symbols belonging to the same OTFS symbol.

2) The amplitude $\bar{g}_{m,n}$ appearing in the RHS of (91) is replaced by the quantity (which is associated with $(p, q) = (m, n)$; see (113))

$$\hat{g}_{m,n}(\mathbf{F}_\tau, \mathbf{F}_\nu) \triangleq \sum_{l=0}^{L-1} \hat{g}_{m,n}(F_{\tau_l}, F_{\nu_l}) = \sum_{l=0}^{L-1} A_l \, \bar{g}_{m,n}(F_{\tau_l}, F_{\nu_l}) \Psi_M(0, -F_{\tau_l}) \Psi_N(0, F_{\nu_l}); \tag{115}$$

here, $\mathbf{F}_\tau \triangleq [F_{\tau_0}, F_{\tau_1}, ..., F_{\tau_{L-1}}]^T$ and $\mathbf{F}_\nu \triangleq [F_{\nu_0}, F_{\nu_1}, ..., F_{\nu_{L-1}}]^T$. Therefore, the amplitude of the term conveying $c_{m,n}$ in $Y[m,n]$ is influenced by all the parameters of the communication channel (namely, its overall number of paths, its Doppler shifts and its path delays).

3) In the presence of a single path (i.e., for $L = 1$), (115) turns into

$$\hat{g}_{m,n}(F_{\tau_0}, F_{\nu_0}) = A_0 \, \bar{g}_{m,n}(F_{\tau_0}, F_{\nu_0}) \Psi_M(0, -F_{\tau_0}) \Psi_N(0, F_{\nu_0}). \tag{116}$$

This shows that, even in the presence of a single propagation path in the communication channel, the amplitude of the term conveying $c_{m,n}$ in $Y[m,n]$ (113) depends not only on $p(t)$ (through $\bar{g}_{m,n}(\cdot, \cdot)$), but also on the path delay and Doppler.

A thorough understanding of the ISI phenomenon affecting $Y[m,n]$ (113) requires analyzing the dependence of function $\Psi_V(v, F)$, that appears in the RHS of (113), on the variable v for a given F. To this aim, it is useful to express the variable F as $F = \bar{F}/V + F_r$, where $\bar{F}$ is an integer and F_r is a real quantity belonging to interval $[-0.5/V, 0.5/V]$ ($\bar{F}$ and F_r represent the so called *integer part* of F and its *fractional part*, respectively). In fact, it is easy to prove that, in general, the function $\Psi_V(v, F)$ exhibits a peak at $v = \bar{F}$ and, if $F_r = 0$, the function $\Psi_V(v, F) = \Psi_V(\bar{F}/V, F)$ turns into a Kronecker delta, i.e.,

$$\delta(v, F) = \begin{cases} 1 & \text{if } v = \bar{F} \\ 0 & \text{otherwise} \end{cases}; \tag{117}$$

otherwise, it exhibits *tails* that decay slowly and that become more pronounced if $|F_r|$ approaches $0.5/V$. Because of the behavior of the function $\Psi_V(v, F)$, the terms $\Psi_M(0, -F_{\tau_l})$ and $\Psi_N(0, F_{\nu_l})$ appearing in the RHS of (113) are responsible for:

1) A *cyclic shift* of all the elements $\{c_{p,q}\}$ of the OTFS symbol matrix $\mathbf{C}$; the horizontal shift and the vertical one are quantified by the integer part of F_{τ_l} and that of F_{ν_l}.

2) The presence of *leakage* (i.e., ISI) when one or both the *fractional* parts of the normalized frequencies F_{τ_l} and F_{ν_l} are different from zero.

Based on these results we can conclude that, even if a DCP is employed, the estimation of the transmitted OTFS symbol requires a form of 2D *equalization*, which is substantially more complicated than its 1D counterparts illustrated for OFDM and DOFDM in the previous two subsections. Equalization, in turn, needs *channel estimation*;

---

[16]In a part of the technical literature on OTFS, the 2D ISI is often split into two components (e.g., see [12]). In practice, on the one hand, the term ISI usually refers to the interference affecting TD samples due to the presence of a fractional component in the delay introduced by the communication channel; on the other hand, the term *inter-Doppler interference* (IDI) is adopted for the interference affecting frequency domain samples due to the presence of a fractional component in the Doppler shift. The 2D ISI turns into *one-dimensional* (1D) ISI in the absence of time dispersion (i.e., multipath) or frequency dispersion (i.e., Doppler).
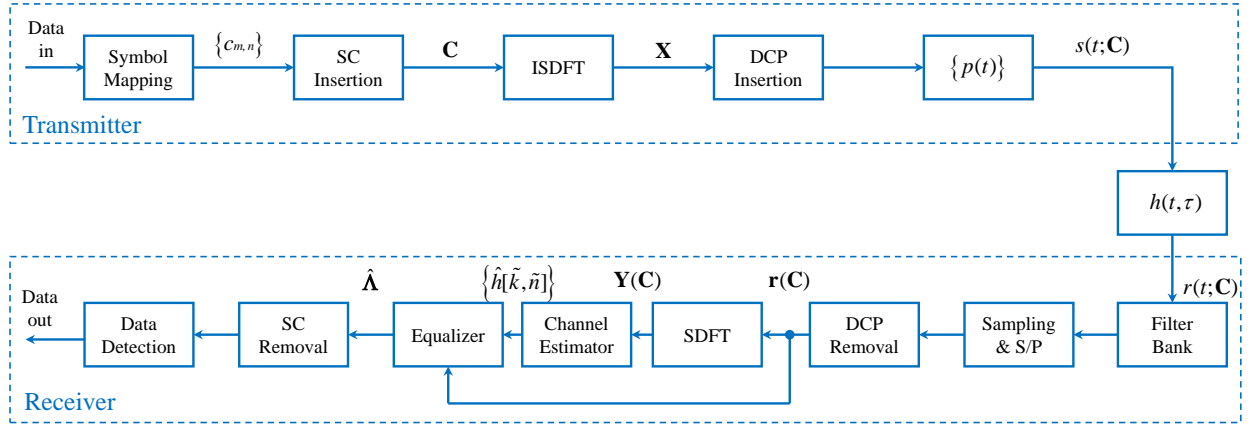
Fig. 1. Baseband model of the developed OTFS-based communication system.

this task is usually accomplished through *pilots*, i.e., through the exploitation of known symbols surrounded by guard symbols (i.e., by zero symbols placed around pilots) for mitigating mutual interference [13], [22].

The baseband architecture of a communication system employing OTFS-DCP and based on the results developed in this paragraph is illustrated in Fig. 1.

4) Pulse-shaping: Let us focus now on the pulse shaping problem, i.e., on how to select the pulse $p(t)$. In the technical literature, the use of a rectangular pulse is often taken into consideration, since its simple shape makes mathematical derivations easier [8], [9], [12], [13], [23]–[25]. However, this choice is not in agreement with the fact that: 1) as illustrated in Paragraph II-C.1, an OTFS signal can be seen as the superposition of multiple OFDM signals, characterized by distinct central frequencies; 2) the generation of an OFDM signal requires the use of a bandlimited pulse, whose amplitude spectrum exhibits a flat top[17] (see Paragraph II-A). Based on these considerations, in our work the following choices have been made:

a) The same pulse as the one adopted in our OFDM signal model has been selected for $p(t)$ (therefore, its spectrum $P(f)$ is expressed by (17)). Note that, for any value of its roll-off factor α, its bandwidth is equal to $(1 + \alpha)/(2T_s)$ and, consequently, never exceeds $\Delta_f = 1/T_s = N/T$.

b) Subcarrier suppression has been employed to ensure that the useful subcarriers of the multiple OFDM signals, which the OTFS signal is made of, have identical amplitudes and that self-interference is avoided (see Subsection II-A).

Regarding point a), if the above mentioned pulse is selected, only the terms associated with $u \in \{-1, 0, 1\}$ survive in the sums appearing in the RHS of (78) and (82), because of the limited bandwidth of $p(t)$. As far as point b) is concerned, instead, following the rules illustrated for OFDM, subcarrier suppression can be achieved by simply setting to zero $N_{sc} \triangleq N - 2N_\alpha - 1$ consecutive columns[18] of the matrix $\mathbf{C}$; this means that

$$\bar{N}_{sc} \triangleq M(N - 2N_\alpha - 1) \tag{118}$$

elements of the matrix $\mathbf{C}$ do not convey channel symbols, being set to zero. Note also that:

a) Subcarrier suppression ensures that, in principle, the coefficients $\{\bar{g}_{m,n}\}$ (see (82)) associated with the unsuppressed channel symbols $\{c_{m,n}\}$ in (88) have exactly the same amplitude (and, in particular, a unitary amplitude for the selected pulse).

b) If this occurs, (92) can be rewritten as

$$x_{m,n} \triangleq \frac{1}{\sqrt{MN}} \sum_{p=0}^{M-1} \sum_{q=-N_\alpha}^{N_\alpha} c_{p,R_N[q]} \exp\left(j2\pi\left(\frac{q}{N}n - \frac{p}{M}m\right)\right), \tag{119}$$

with $m = 0, 1, ..., M - 1$ and $n = 0, 1, ..., N - 1$.

---

[17] As already observed in Subsection II-A, this choice ensures that the useful (i.e., unsuppressed) subcarriers of an OFDM signal have the same amplitude.

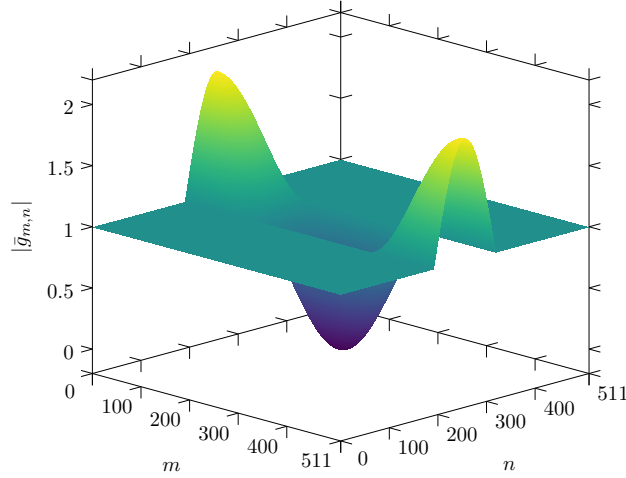[18] In particular, the columns whose index runs from $N_\alpha + 1$ to $N - N_\alpha - 1$.

Fig. 2. Representation of the 2D sequence $\{|\bar{g}_{m,n}|\}$ for $M = N = 512$. The spectrum $P(f)$ is expressed by (17) with $\alpha = 0.25$.
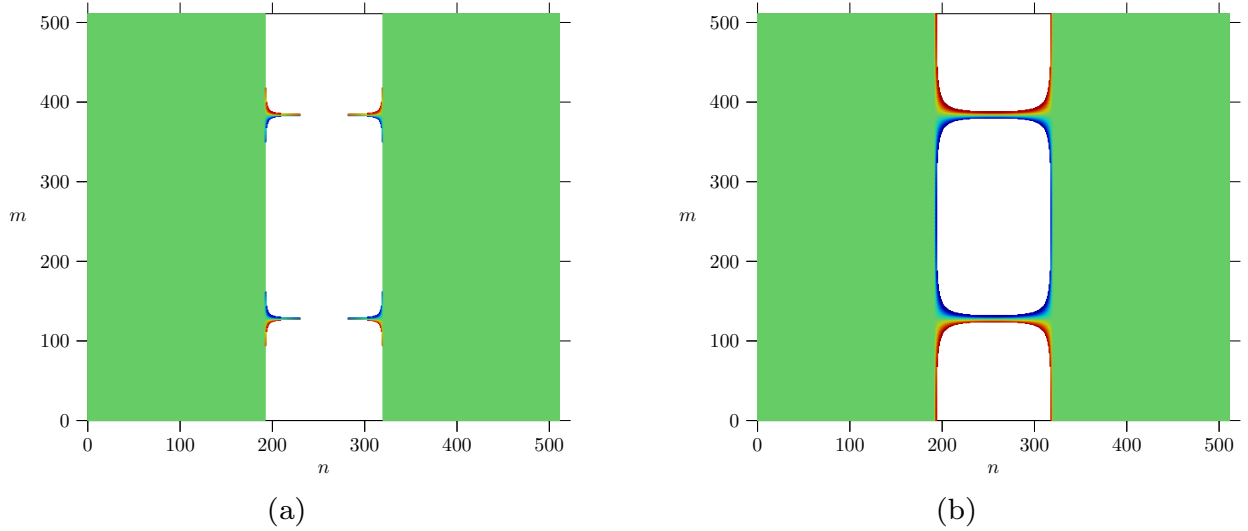

| (a) | (b) |

Fig. 3. Heat maps representing the behavior of the sequence $\{|\bar{g}_{m,n}|\}$ in the 2D region $\Gamma_\varepsilon(\alpha)$ (120) for a) $\varepsilon = 0.01$ and b) $\varepsilon = 0.05$; $\alpha = 0.25$ is assumed in both cases.

The overall number of channel symbols conveyed by a single OTFS symbol can be increased a little bit by relaxing the above mentioned amplitude constraint at the price of introducing a limited amount of self-interference. In the considered case, this result can be achieved by exploiting all the elements of the matrix $\mathbf{C}$ whose indexes (m, n) belong to the set

$$\Gamma_\varepsilon(\alpha) \triangleq \{(m, n) : (1 - \varepsilon) \le |\bar{g}_{m,n}| \le (1 + \varepsilon)\};\tag{120}$$

here, $m = 0, 1, ..., M - 1$, $n = 0, 1, ..., N - 1$ and ε denotes a real (and small) positive parameter representing the maximum tolerable deviation from a unitary amplitude. These concepts are exemplified by Fig. 2, in which the amplitude of the complex 2D sequence $\{\bar{g}_{m,n}\}$ is represented for $M = N = 512$ and $\alpha = 0.25$. In this case, if $\varepsilon = 0$ is selected, 386 subcarriers are available for data transmission. On the other hand, if $\varepsilon = 0.01$ and $\varepsilon = 0.05$ are chosen, the overall number of useful subcarriers increases to 388 and 401, respectively. The small increase observed in this case is due to the fast variations observed in the sequence $\{|\bar{g}_{m,n}|\}$ out of its flat region; this is evidenced by the two heat maps shown in Fig. 3, that represent the behavior of the sequence $\{|\bar{g}_{m,n}|\}$ in the 2D region $\Gamma_\varepsilon(\alpha)$ (120) for $\varepsilon = 0.01$ and $\varepsilon = 0.05$. Note also that a larger cardinality of the set $\Gamma_\varepsilon(\alpha)$ results in a higher transmission rate; the impact of the roll-off factor on this can be assessed by evaluating the *spectral efficiency* (SE) [8], [10]

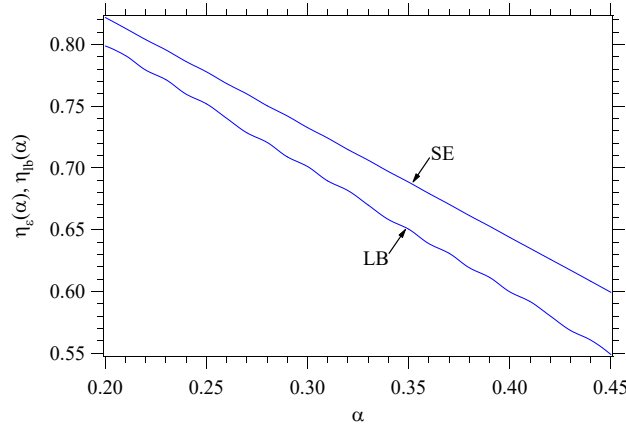$$\eta_\varepsilon(\alpha) \triangleq \frac{N_\varepsilon(\alpha)}{MN},\tag{121}$$

Fig. 4. Representation of $\eta_\varepsilon(\alpha)$ (121) (SE) and its lower bound $\eta_{\text{lb}}(\alpha)$ (122) (LB) versus α for $\alpha \in [0.2; 0.45]$; $\varepsilon = 0.05$ and $M = N = 512$ have been selected.

where $N_\varepsilon(\alpha)$ denotes the cardinality of the set $\Gamma_\varepsilon(\alpha)$ (120) (i.e., the overall number of useful channel symbols conveyed by a single OTFS symbol). A representation of $\Gamma_\varepsilon(\alpha)$ and that of its *lower bound* (LB)

$$\eta_{\text{lb}}(\alpha) \triangleq \frac{(2N_\alpha + 1)M}{MN} = \frac{2N_\alpha + 1}{N} \tag{122}$$

versus α is provided in Fig. 4 for $\alpha \in [0.2; 0.45]$; $\varepsilon = 0.05$ and $M = N = 512$ have been selected in this case. From this figure it is easily inferred that reducing α improves the spectral efficiency of the communication system; this is due to the decrease of the overall number of SCs. However, this result is achieved at the price of an increase in the duration of $p(t)$ and, consequently, of a longer CP in the TD (i.e., in a higher value of $N_{cp}^{(\text{TD})}$).

The considerations made in this paragraph until this point refer to the inner structure of the transmitted signal. As shown in Paragraph II-C.3, this structure may be substantially modified by a doubly selective communication channel. In particular, as illustrated at the end of that paragraph, the complex amplitude $\bar{g}_{m,n}$ associated with the channel symbol $c_{m,n}$ in $Y[m,n]$ (91) is replaced by $\hat{g}_{m,n}(F_{\tau_0}, F_{\nu_0})$ (see (116)) in the presence of a single path in the communication channel (i.e., for $L = 0$). Let us now analyze the impact of this simple communication channel on the transmitted signal under the assumption that, once again, $P(f)$ is expressed by (17). Some numerical results referring to the considered scenario are shown in Fig. 5, in which the amplitude of the complex factor $\hat{g}_{m,n}(F_{\tau_0}, F_{\nu_0})$ versus n is illustrated under the assumption that: 1) $M = N = 512$; 2) $T_s = 4$ µs; 3) path gain $A_0 = 1$; 4) $F_{\tau_0} = 4 \cdot 10^{-4}$ (this value corresponds to the path length $R_0 = 250$ m); 5) $F_{\nu_0} = 0.0222$ (this value corresponds to the velocity $v = 250$ km/h if the carrier frequency $f_c = 24$ GHz is employed); 6) $\alpha = 0.25$; 7) $m = M/2 - 1$ (this choice allows us to asses the impact of the Doppler introduced by the communication channel on a specific row of the $M \times N$ matrix $[\hat{g}_{m,n}(F_{\tau_0}, F_{\nu_0})]$). Comparing the amplitude $|\hat{g}_{M/2-1,n}(F_{\tau_0}, F_{\nu_0})|$ with its counterpart $|\bar{g}_{M/2-1,n}|$ referring to an ideal scenario leads to the conclusion that, in the considered case, such amplitudes are close; moreover, similar results are observed for other values of m. Our numerical results have also evidenced that limited changes are also observed in the phase of the sequence $\{\hat{g}_{M/2-1,n}(F_{\tau_0}, F_{\nu_0})\}$ with respect to the phase of $\{\bar{g}_{M/2-1,n}\}$ in the flat region of its amplitude. Based on these results, we can assume that

$$\bar{g}_{p,q}(F_{\tau_l}, F_{\nu_l}) \cong \bar{g}_{p,q} \tag{123}$$

for any l and (p, q). This approximation, obtained for a specific pulse, has the following relevant implications: 1) the SC positions can be unambiguously identified at the RX side; 2) the approximation

$$T_l[\tilde{k}, \tilde{n}] \cong T[\tilde{k}, \tilde{n}] = \frac{1}{\sqrt{MN}} \sum_{p=0}^{M-1} \sum_{q=0}^{N-1} c_{p,q} \bar{g}_{p,q} \cdot \exp\left(-j2\pi\left(\frac{p}{M}\tilde{k} - \frac{q}{N}\tilde{n}\right)\right) \tag{124}$$

can be adopted in the RHS of (110), so that (see (111))

$$r[\tilde{k}, \tilde{n}] \cong T[\tilde{k}, \tilde{n}] h[\tilde{k}, \tilde{n}], \tag{125}$$
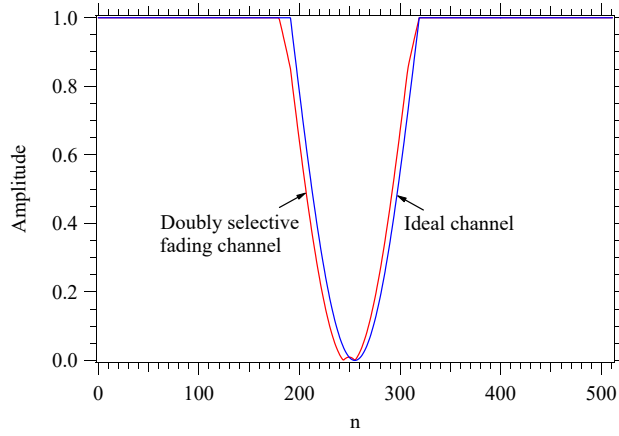
Fig. 5. Representation of the sequences $\{|\hat{g}_{M/2-1,n}(F_{\tau_0}, F_{\nu_0})|\}$ and $\{|\bar{g}_{M/2-1,n}|\}$; a single path doubly selective fading channel characterized by $A_0 = 1$ and $(F_{\tau_0}, F_{\nu_0}) = (4 \cdot 10^{-4}, 0.0222)$ is assumed in the evaluation of the first sequence. Here $M = N = 512$ and a roll-off value $\alpha = 0.25$ are assumed.

where (see (109))

$$h[\tilde{k}, \tilde{n}] \triangleq \sum_{l=0}^{L-1} h_l[\tilde{k}, \tilde{n}] = \sum_{l=0}^{L-1} A_l \exp\big(-j2\pi\tilde{k}F_{\tau_l}\big) \exp(j2\pi\tilde{n}F_{\nu_l}) \tag{126}$$

represents the multiplicative distortion introduced by the communication channel. Note that, if (125) holds, channel equalization is tantamount to compensating for the factor $h[\tilde{k}, \tilde{n}]$ (126) appearing in the RHS of that equation.

Since the selection of $p(t)$ influences the structure of the OTFS signal (63), it should be expected that it has a major impact on the spectral properties of that modulation format. In Appendix D, the derivation of the PSD $S_s(f)$ of the OTFS complex envelope $s(t; \mathbf{C})$ (63) is sketched for the pulse shape considered in this paragraph; in particular, it is shown that

$$S_s(f) = \sum_{k=-(M/2+N_{cp}^{(\mathrm{FD})})}^{M/2-1+N_{cpo}^{(\mathrm{FD})}} S_{s_k}(f), \tag{127}$$

where

$$S_{s_k}(f) = \frac{\sigma_c^2}{T(N + N_{cp}^{(\mathrm{TD})})} \big|P\big(f - k\Delta_f\big)\big|^2 \sum_{l=-N_\alpha}^{N_\alpha} S_{s_{k,l}}(f) \tag{128}$$

is the PSD of the signal $s_k^{(\mathrm{TD})}(t; \mathbf{C}))$ (65), σ_c^2 is the variance of the channel symbol constellation[19] and

$$S_{s_{k,l}}(f) = \frac{\sin^2\Big(\pi(N + N_{cp}^{(\mathrm{TD})})(f - k\Delta_f - f_l)T_s\Big)}{\sin^2(\pi(f - k\Delta_f - f_l)T_s)} \tag{129}$$

is the contribution of the lth subcarrier[20] of $s_k^{(\mathrm{TD})}(t; \mathbf{C}))$, to the PSD $S_{s_k}(f)$ (128).

It is important to point out that:

1) If the pulse $p(t)$ selected for the OTFS signal is bandlimited, the OTFS spectrum $S_s(f)$ (127) is also bandlimited (see (128)).

2) The superposition of multiple subcarriers in $S_{s_{k,l}}(f)$ (129) results in the presence of fast oscillations appearing in the overall PSD $S_s(f)$ (127) within its lower and upper band limits (see Fig. 7 in Section IV).

3) The bandwidth B_s of the OTFS-DCP format can be approximated as

$$B_s \cong (M + N_{cp}^{(\mathrm{FD})} + N_{cpo}^{(\mathrm{FD})})\Delta_f. \tag{130}$$

---

[19]The expression of σ_c^2 for different types of constellation can be found in [6, Subsect. (3.5.4)].

[20]This subcarrier is characterized by the frequency $f_{k,l} \triangleq k\Delta_f + l/T = k\Delta_f + l/(NT_s)$.

III. PILOT-AIDED CHANNEL ESTIMATION & EQUALIZATION

In this section, we first focus on the problem of pilot arrangement in data-aided channel estimation for the OTFS-based communication system illustrated in the previous section. Then, we develop a novel approach to data-aided channel estimation and equalization; our approach to channel estimation is based on the observation that, in the considered system, the communication channel in the DD domain can be represented as the superposition of 2D complex exponentials. Finally, the developed technique is compared with two technical alternatives available in the literature.

A. Pilot Arrangement for Channel Estimation

Our channel estimation algorithm relies on the transmission of N_{pil} pilot channel symbols in each OTFS symbol. Moreover, each pilot channel symbol is surrounded by a *rectangular guard*, containing multiple null symbols[21]. In practice, if x_v and (p_v, q_v) denote the vth pilot channel symbol (with $v = 0, 1, ..., N_{\text{pil}} - 1$) and its coordinates within the $M \times N$ OTFS symbol matrix $\mathbf{C} = [c_{p,q}]$ (with $(p_v, q_v) \in \Gamma_\varepsilon(\alpha)$; see (120)), we have that

$$c_{p,q} = 0 \tag{131}$$

for any $(p, q) \in \Gamma_{\text{g}}^{(v)} \setminus \{(p_v, q_v)\}$, where

$$\Gamma_{\text{g}}^{(v)} \triangleq \{(R_M[p_v + k], R_N[q_v + l]); |k| \leq p_\tau, |l| \leq 2q_\nu\}; \tag{132}$$

here, p_τ and q_ν are integer parameters defining the vertical width and the horizontal width, respectively, of the rectangular guard. Based on all this, we can state that the allocation of N_{pil} pilot symbols to the same OTFS symbol entails the introduction of

$$N_{\text{g}} \triangleq N_{\text{pil}}[(2p_\tau + 1)(4q_\nu + 1) - 1] \tag{133}$$

guard symbols. The transmission rate of the considered communication system can be maximized by: 1) minimizing N_{g} as much as possible; 2) exploiting, as guardbands, the portions of $\mathbf{C}$ zeroed for subcarrier suppression. As far as point 1) is concerned, it should be kept in mind that p_τ and q_ν cannot be arbitrarily small, since their values should be selected on the basis of the maximum delay $\tau_{\max}$ and the maximum Doppler shift $\nu_{\max}$, respectively, envisaged for the communication channel[22]. More specifically, we should select

$$p_\tau = \lceil \tau_{\max}/\tau_{\text{res}} \rceil \tag{134}$$

and

$$q_\nu = \lceil \nu_{\max}/\nu_{\text{res}} \rceil, \tag{135}$$

where $\lceil \cdot \rceil$ denotes the ceiling operator, whereas $\tau_{\text{res}} \triangleq T_s/M$ and $\nu_{\text{res}} \triangleq \Delta_f/N$ represent the *delay resolution* and *Doppler frequency resolution*, respectively. If these choices are made, we can extract, from the DD domain matrix $\mathbf{Y}(\mathbf{C})$ (112), N_{pil} distinct $P \times Q$ submatrices, each containing a symbol; here,

$$P \triangleq p_\tau + 1 \tag{136}$$

and

$$Q \triangleq 2q_\nu + 1. \tag{137}$$

are selected in a way that no information symbol has stepped inside each submatrix because of path delays and/or Doppler shifts (further details are provided below), so that its content depends on a single pilot channel symbol only.

It is easy to understand that the elements of $\mathbf{C}$ that are not occupied by the N_{pil} pilots or their guards, or are not in use for subcarrier suppression (see Subsection II-C.4) can be exploited to convey information symbols. These concepts are exemplified by Fig. 6, which refers to an OTFS symbol characterized by $M = N = 32$. In this case, $N_{\text{pil}} = 4$ pilot symbols are transmitted and the guardband associated with each of them is characterized by $p_\tau = 4$ and $q_\nu = 1$.

---

[21]In our communication system, the pilot configuration is assumed to be time invariant, meaning it does not change over consecutive OTFS symbols.

[22]Do not forget that the presence of a delay and a Doppler shift results in a 2D cyclic shift of all the elements of the each OTFS symbol. In the following, we assume that $\tau_{\max}$ and $\nu_{\max}$ do not exceed $T_s/2$ and $\Delta_f/2$, respectively, in order to avoid any ambiguity in the interpretation of detected OTFS symbols.
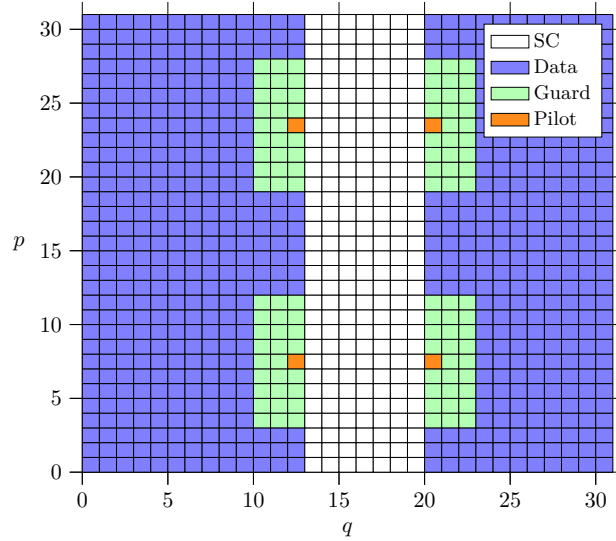
Fig. 6. Pilot arrangement in an OTFS symbol characterized by $M = N = 32$. Each guardband partially overlaps with the portion of the OTFS symbol zeroed because of subcarrier suppression.

It is important to point out that:

1) In general, the *transmission rate loss* due to the pilot arrangement scheme exemplified by Fig. 6 can be quantified by evaluating the parameter

$$\Lambda_{\text{pil}} \triangleq \frac{N_g}{MN}, \tag{138}$$

that represents the fraction of channel symbols that are not exploited for data transmission (note that the presence of SCs is ignored).

2) The transmitted pilots can be used not only for channel estimation at the RX side, but also for target detection and estimation at the TX side in a wireless system accomplishing *joint communication and sensing* (JCAS).

3) The pilot arrangement described above is conceptually related to that illustrated in [8, Fig. 1], where, however, the use of a single pilot only in each OTFS symbol is taken into consideration.

4) In various manuscripts pilot channel symbols are arbitrarily positioned in the matrix $\mathbf{C}$ (e.g., see [24], [25]). In Paragraph II-C.4 we have shown that pilot positioning cannot be arbitrary and is influenced by pulse shaping, since subcarrier suppression can never be ignored.

B. Channel Estimation and Equalization

Let us focus now on the problem of estimating the inner structure of the communication channel; this requires estimating the L triplets $\{(A_l, F_{\tau_l}, F_{\nu_l}); l = 0, 1, ..., L - 1\}$ and the parameter L; in fact, these provide a full description of the communication channel, described by the $M \times N$ matrix $\mathbf{h} \triangleq [h[\tilde{k}, \tilde{n}]]$ (see (126)).

First of all, let us assume, for simplicity, that the matrix $\mathbf{C}$ conveys a *single pilot channel symbol* (denoted x_0 and having coordinates $(p_0, q_0) \in \Gamma_\varepsilon(\alpha)$) and that all the remaining elements of it form the guardband of that symbol (this scenario is denoted *full guard*, FG, in the following). Under this assumption, based on (123), the element $(\tilde{k}, \tilde{n})$ of the channel matrix $\mathbf{h}$ can be approximately expressed as[23] (see (124) and (125))

$$h[\tilde{k}, \tilde{n}] \cong \hat{h}[\tilde{k}, \tilde{n}] \triangleq \frac{\sqrt{MN}}{x_0} \exp\left(j 2\pi \left(\frac{p_0}{M}\tilde{k} - \frac{q_0}{N}\tilde{n}\right)\right) r[\tilde{k}, \tilde{n}]. \tag{139}$$

From the last equation it is easily inferred that an estimate $\hat{h}[\tilde{k}, \tilde{n}]$ of the element $(\tilde{k}, \tilde{n})$ of $\mathbf{h}$ can be easily evaluated on the basis of the received signal $r[\tilde{k}, \tilde{n}]$, for any $\tilde{k}$ and $\tilde{n}$ (see (125)). Note that:

---

[23]The term $\bar{g}_{p_v, q_v}$ (with $v = 0$) does not appear in the RHS of (139), as its value for any couple of indices $(p, q) \in \Gamma_\varepsilon(\alpha)$ (120) is assumed to be unitary. The same assumption is also made in the following for any v.

1) The set of complex gains $\{\hat{h}[\tilde{k}, \tilde{n}]\}$ does not directly provide a full knowledge of the communication channel, since the channel inner structure, in terms of number of paths, delays and Doppler shifts, cannot be immediately inferred from that set. For this reason, in the following this set is considered as a form of partial CSI[24].

2) Thanks to (126), the 2D sequence $\{\hat{h}[\tilde{k}, \tilde{n}]\}$ can be seen as the noisy superposition of 2D complex exponentials whose parameters (namely, complex amplitude and normalized frequencies) completely describe the inner structure of the communication channel. For this reason, the set of those parameters can be considered as a form of *full* CSI, that can be acquired by applying the 2D sequence $\{\hat{h}[\tilde{k}, \tilde{n}]\}$ to an algorithm for *multidimensional harmonic retrieval* (MHR, e.g., see [26] and references therein).

3) The FG option described above should be only taken into consideration in two distinct scenarios. In the first scenario, a single OTFS (pilot) symbol is transmitted for sensing purposes only. In the second one, instead, the OTFS pilot symbol is part of a frame and is followed by multiple OTFS symbols conveying data; in this case, the channel estimates evaluated on the basis of the pilot symbol are used as they are for channel equalization if channel changes are deemed negligible over the whole frame or to initialize decision-directed channel tracking if the last assumption does not hold.

In the remaining part of this manuscript, we do not take into consideration the FG option again. In fact, we focus on a specific scenario, characterized by the transmission of a single OTFS symbol conveying both information symbols and multiple (namely, N_{pil}) pilot symbols for improving the quality of channel estimates at a low *signal-to-noise ratio* (SNR; see Paragraph III-A). Moreover, we concentrate on the problem of estimating the full CSI from the noisy matrix

$$\mathbf{Z}(\mathbf{C}) \triangleq [Z[p,q]] = \mathbf{Y}(\mathbf{C}) + \mathbf{W}_{M,N}, \tag{140}$$

where $\mathbf{Y}(\mathbf{C})$ (112) represents the useful part of $\mathbf{Z}(\mathbf{C})$, $\mathbf{W}_{M,N}$ is a complex $M \times N$ noise matrix whose (p,q)th element $W[p,q]$ is the noise sample affecting $Z[p,q]$ (an *additive white Gaussian noise*, AWGN, model is assumed for the 2D sequence $\{W[p,q]\}$; moreover, the variance of each element of that sequence is denoted σ^2). The channel estimation method we propose extracts the full CSI from $N_{\mathrm{pil}} P \times Q$ non-overlapping submatrices, denoted $\{\mathbf{Z}^{(v)}; v = 0, 1, ..., N_{\mathrm{pil}} - 1\}$; the vth submatrix $\mathbf{Z}^{(v)}$ is obtained from $\mathbf{Z}(\mathbf{C})$ (140) by: 1) extracting all the elements whose coordinates (p,q) belong to the set

$$\Gamma_{\mathrm{w}}^{(v)} \triangleq \{(R_M[p_v + k], R_N[q_v + l]); 0 \le k \le p_\tau, |l| \le q_\nu\}, \tag{141}$$

where p_τ and q_ν are defined by (134) and (135), respectively; 2) renumbering the extracted elements in a way that the new row and column indices run from 0 to $P - 1$ and from 0 to $Q - 1$, respectively. This allows us to approximate the element (p', q') of $\mathbf{Z}^{(v)}$ as (see (113) and (123))

$$Z^{(v)}[p', q'] \cong \frac{1}{MN} x_v \left[\sum_{l=0}^{L-1} A_l \Psi_M \left(p', -F_{\tau_l} \right) \cdot \Psi_N \left(q' - q_\nu, F_{\nu_l} \right) \right] + W[p', q'], \tag{142}$$

with $p' = 0, 1, ..., P - 1$ and $q' = 0, 1, ..., Q - 1$. Note that the rule defined above for element selection ensures that the submatrix $\mathbf{Z}^{(v)}$ depends on the vth pilot symbol only, provided that the leakage affecting $\mathbf{Z}^{(v)}$ in the DD domain (see (113)) and originating from close data symbols is negligible. Moreover, the choice of the parameters P and Q (see (136) and (137), respectively) also implies that pilot channel symbols can not step outside each submatrix; in other words, each submatrix $\mathbf{Z}^{(v)}$ embeds all the channel effects (i.e., 2D shifts).

Given the set $\{\mathbf{Z}^{(v)}; v = 0, 1, ..., N_{\mathrm{pil}} - 1\}$, the estimation of the inner structure of the communication channel can be accomplished by sequentially executing the three steps described below (the ith Step is denoted **S1** in the following).

S1) The estimate

$$\hat{\mathbf{h}}_{\mathrm{w}} = \mathrm{ISDFT}_{P,Q}[\hat{\mathbf{H}}_{\mathrm{w}}], \tag{143}$$

of the $P \times Q$ matrix $\mathbf{h}_{\mathrm{w}}$ is computed; here,

$$\hat{\mathbf{H}}_{\mathrm{w}} = \frac{1}{N_{\mathrm{pil}}} \sum_{v=0}^{N_{\mathrm{pil}}-1} \frac{\mathbf{Z}^{(v)}}{x_v} \tag{144}$$

---

[24]Another form of partial CSI is represented by the SDFT of $\{\hat{h}[\tilde{k}, \tilde{n}]\}$, i.e., its DD domain representation.

is a $P \times Q$ matrix; moreover, the element (p', q') of $\mathbf{Z}^{(v)}$ is expressed by (142).

S2) The matrix $\hat{\mathbf{h}}_{\mathrm{w}}$ (143) is processed by an algorithm for 2D MHR; this produces an estimate $\hat{L}$ of L and the estimates $\{(\hat{A}_l, \hat{F}_{\tau_l}, \hat{F}_{\nu_l}); l = 0, 1, ..., \hat{L} - 1\}$ of the parameters (namely, complex amplitude and normalized frequencies) characterizing the $\hat{L}$ detected complex exponentials.

S3) An estimate $\hat{\mathbf{h}} \triangleq [\hat{h}[\tilde{k}, \tilde{n}]]$ of the channel matrix $\mathbf{h}$ is evaluated by means of (126) for $\tilde{k} = 0, 1, ..., M - 1$ and $\tilde{n} = 0, 1, ..., N - 1$; $F_{\tau_l} = \hat{F}_{\tau_l}$, $F_{\nu_l} = \hat{F}_{\nu_l}$, $A_l = \hat{A}_l$ and $L = \hat{L}$ are assumed in this case.

The overall procedure described above deserves the following comments:

1) The choice of the parameters P and Q (see (136) and (137), respectively) allows us to extract the channel parameters on the basis of a $P \times Q$ matrix (namely, $\mathbf{h}_{\mathrm{w}}$; see (143)) instead of an $M \times N$ one (namely, $\mathbf{h}$).

2) The set $\{\mathbf{Z}^{(v)}; v = 0, 1, ..., N_{\mathrm{pil}} - 1\}$ consists of N_{pil} submatrices affected by both additive noise and interference; the last phenomenon is due to the leakage appearing in the presence of fractional delays and Dopplers; evaluating the sum that appears in the RHS of (144) aims at improving the quality of channel estimates at low SNR through the constructive combination of multiple submatrices.

3) In our computer simulations, the *complex single frequency-delay estimation and cancellation* (CSFDEC) algorithm [18] has been employed for MHR in **S2**. This choice is motivated by the fact that the CSFDEC algorithm may perform substantially better than other estimators in the presence of multiple closely spaced tones and is able to generate an estimate of L (i.e., it does not require prior knowledge about the overall number of superimposed tones).

4) The estimates of the parameters (namely, complex amplitude and normalized frequencies) describing the structure of the communication channel computed in **S2** can be employed for target detection and estimation in JCAS systems.

5) The normalized frequencies generated by the adopted MHR algorithm need to be properly scaled since this algorithm processes the $P \times Q$ matrix $\hat{\mathbf{h}}_{\mathrm{w}}$ (143). More precisely, for any l, the normalized frequencies $\hat{F}_{\tau_l}$ and $\hat{F}_{\nu_l}$ provided by that algorithm need to be multiplied by P/M and Q/N, respectively, before being employed in the evaluation of the estimate $\hat{\mathbf{h}}$ in **S3**.

The estimate $\hat{\mathbf{h}}$, made available by **S3**, can be employed for channel equalization and symbol detection; the first task requires sequentially accomplishing the three steps described below (the ith Step is denoted **Ei** in the following).

E1) *Evaluation of the equalizer gains* - The *minimum mean square error* (MMSE) gain

$$G_{\mathrm{mmse}}[\tilde{k}, \tilde{n}] = \hat{h}^*[\tilde{k}, \tilde{n}]\left(\hat{h}[\tilde{k}, \tilde{n}]\hat{h}^*[\tilde{k}, \tilde{n}] + \hat{\sigma}^2\right)^{-1} \tag{145}$$

is evaluated for channel equalization; here, $\tilde{k} = 0, 1, ..., M - 1$ and $\tilde{n} = 0, 1, ..., N - 1$, and $\hat{\sigma}^2$ represents an estimate of the variance of the noise affecting $\mathbf{Z}(\mathbf{C})$ (140).

E2) *Channel Equalization* - The estimate

$$\hat{T}[\tilde{k}, \tilde{n}] = r[\tilde{k}, \tilde{n}] \, G_{\mathrm{mmse}}[\tilde{k}, \tilde{n}], \tag{146}$$

of $T[\tilde{k}, \tilde{n}]$ (124) is computed for $\tilde{k} = 0, 1, ..., M - 1$ and $\tilde{n} = 0, 1, ..., N - 1$. All the estimates $\{\hat{T}[\tilde{k}, \tilde{n}]\}$ are collected in the $M \times N$ matrix $\hat{\mathbf{T}}$.

E3) *From TF domain to DD domain* - The $M \times N$ matrix

$$\hat{\mathbf{\Lambda}} = \mathrm{SDFT}_{M,N}[\hat{\mathbf{T}}], \tag{147}$$

is evaluated in order to go back to the DD domain, i.e., to the domain in which symbol detection is accomplished.

Finally, all the elements of the matrix $\hat{\mathbf{\Lambda}}$ associated with the suppressed channel symbols are discarded, whereas the remaining elements[25] undergo data detection. This produces the estimate $\hat{c}_{m,n}$ of $c_{m,n}$ for any $(m, n) \in \Gamma_\varepsilon(\alpha)$.

The algorithm illustrated above and dubbed *multiple tone estimation* and *equalization* (MTEE) in the following deserves the following comments:

1) If the residual parts of all the normalized delays and normalized Doppler shifts were equal to zero (i.e., if the quantities $F_{\tau_l} M$ and $F_{\nu_l} N$ are integer for $l = 0, 1, ..., L - 1$), the matrix $\hat{\mathbf{h}}$ could be replaced by the $P \times Q$) matrix $\hat{\mathbf{h}}_{\mathrm{w}}$ (see (143)) in the evaluation of the equalizer gains (see (145) in **E1**). For this reason, in

---

[25]All these elements are associated with the set of indexes $\{(m, n) \in \Gamma_\varepsilon(\alpha)\}$ (see (120)).

this case, **S2** and **S3** should not be executed. Note, however, that the order (P,Q) ISDFT in (143) should be replaced by an order (M,N) ISDFT.

2) The computational cost of MMSE equalization is $N_{\mathrm{mmse}} = N_{\mathrm{eq}} + N_{\mathrm{dd}}$, where $N_{\mathrm{eq}} = \mathcal{O}(MN)$ and $N_{\mathrm{dd}} = \mathcal{O}(MN\log_2(MN))$ are the costs of computing (145)-(146) and (147), respectively. From the last result, it can be inferred that the overall computational cost of the MMSE equalizer is approximately of order $\mathcal{O}(N_{\mathrm{mmse}})$, where

$$N_{\mathrm{mmse}} = MN\log_2(MN). \tag{148}$$

3) The computational cost of the proposed equalization method (see **E1**-**E3**) is much lower than that required by the MMSE or *zero-forcing* (ZF) techniques operating in the DD domain and adopted in [13], [23]; in fact, these involve matrix inversion (as opposed to element-wise division in (146)) and thus require $\mathcal{O}((MN)^3)$ operations (e.g., see [13, Eq. (48)]).

C. Comparison with other channel estimation & equalization techniques

The technique for channel estimation & equalization described in Paragraph III-B is conceptually related to: a) the threshold-based approach developed by Raviteja *et al.* [8] and denoted Alg-R in the following; b) the frequency estimation algorithm proposed by *Wu et al.* [16] and denoted Alg-W in the following. In fact, all these algorithms rely on the transmission of pilot symbols to extract partial or full CSI. Despite their similarities, they exhibit various differences concerning the six specific issues listed below.

1) *Assumptions on delays and Doppler shifts*: Alg-R has been developed under the restrictive assumption that the fractional part of all normalized delays is equal to zero. This assumption does not hold, instead, for the derivation of MTEE algorithm and Alg-W. Keep in mind that the presence of a fractional part in normalized delays makes the problems of channel estimation and data detection significantly more challenging.

2) *Pilot symbol arrangement*: In Alg-R and Alg-W, a single pilot symbol is employed for channel estimation (e.g. see [8, Figs. 1-2]); moreover, its position does not take into account the impact of pulse shaping illustrated in Subsection II-C.4. The MTEE algorithm, instead, can benefit from the use of multiple pilot symbols, whose position is carefully selected on the basis of the adopted pulse shape and the suppressed channel symbols.

3) *Channel estimation method*: The channel estimation technique proposed in Alg-R exploits a threshold-based approach to extract partial CSI (represented by the matrix $\hat{\mathbf{H}}_{\mathrm{w}}$) only; then, these information are exploited in an iterative data detection process. On the other hand, a DFT-based approach initialized through Alg-R is employed by Alg-W. The last algorithm is able, similarly as the MTEE algorithm, to estimate both integer and fractional components of normalized delays and normalized Doppler shifts (see the frequency estimation algorithm described in [16, Sec. IV-A]).

4) *Use of channel estimates for sensing purposes*: Even if the exploitation of the channel estimates generated by Alg-R for sensing purposes has not been investigated in [8], the threshold-based approach on which this algorithm is based paves the way for the estimation of the integer parts of normalized delays and Doppler shifts; these can be considered as *coarse* estimates of target parameters. Alg-W, instead, has been proposed for sensing only; for this reason, it does not solve the problems of channel equalization and data detection. On the other hand, the MTEE algorithm can be employed for JCAS in the proposed OTFS-DCP-based communication system.

5) *Equalization technique*: A message passing detection and interference cancellation algorithm to be used jointly with Alg-R has been developed in [12]; it relies on a *sparse model* of the received signal. Sparsity entails a significant reduction in the complexity of iterative detection methods. However, if the RX signal matrix in the TF domain or in the DD one is not sufficiently sparse (because of the presence of fractional components in the channel delays and/or Doppler shifts [13], [22]), iterative detectors become infeasible because of their highly increasing complexity, may produce significant detection errors and may not even converge. On the other hand, the MTEE algorithm is not based on a sparse signal model (see (125)); moreover, it makes use of an MMSE equalizer, fed by the full CSI (represented by the set $\{(\hat{A}_l, \hat{F}_{\tau_l}, \hat{F}_{\nu_l}); l = 0, 1, ..., \hat{L}-1\}$ and the parameter $\hat{L}$; see **Se2**). Finally, in the development of Alg-W, the problem of equalization has not been considered.

6) *Computational complexity*: The computational complexity orders of Alg-R, MTEE and Alg-W are listed in Table I, where the partial contributions due to *channel estimation*, *sensing* and *equalization* steps are also provided. From the provided formulas, the following conclusions can be easily inferred:

TABLE I
COMPUTATIONAL COMPLEXITY ORDER OF ALG-R, MTEE AND ALG-W.

Technique	Channel estimation $\mathcal{O}(\cdot)$	Sensing $\mathcal{O}(\cdot)$	Equalization $\mathcal{O}(\cdot)$
Alg-R	PQ	–	MNS
MTEE	$(N_{\mathrm{pil}} + \log_2(PQ))PQ$	$13\big[P_0Q_0\log_2(P_0Q_0) + L^2N_{\mathrm{it}}N_{\mathrm{ref}}I_{\mathrm{p}}I_{\mathrm{q}}\big]$	$MN\log_2(MN)$
Alg-W	$(1 + \log_2(PQ))PQ$	$P_0Q_0\log_2(P_0Q_0) + LN_{\mathrm{it}}8PQ$	–

a) In channel estimation, Alg-R evaluates the matrix $\hat{\mathbf{H}}_{\mathrm{w}}$ (144) only under the assumption that a single pilot symbol is transmitted (i.e., $N_{\mathrm{pil}} = 1$). On the other hand, both the MTEE algorithm and Alg-W require also the estimation of the matrix $\hat{\mathbf{h}}_{\mathrm{w}}$ (143), which is processed by an MHR algorithm for sensing purposes. The only difference between the MTEE algorithm and Alg-W is represented by the fact that the last method uses a single pilot for channel estimation.

b) The computational cost of the sensing step of the MTEE algorithm (see [26, eq. (55)]) is given by the sum of different contributions. The first contribution is the cost of *initialization*; this requires the evaluation of the order (P_0, Q_0) SDFT of $\hat{\mathbf{h}}_{\mathrm{w}}$ (143) and its first three derivatives[26]. In general, $P_0 \geq P$ and $Q_0 \geq Q$, since *oversampling* is employed along one or both dimensions in order to improve the sensing accuracy. The second contribution, instead, is given by the cost of *refinements*; the cost of each refinement depends on the overall number of targets L and on the interpolation technique[27] adopted in each refinement step of the CSFDEC algorithm employed for MHR in **S2**. Note that the overall refinement step can be run N_{ref} times.

c) The Alg-W cost (see [16, Sec. IV-B]) also results from the sum of the costs of its initialization (requiring the evaluation of a single 2D spectrum) with that of an iterative refinement step based on DFT coefficients.

d) In accomplishing channel equalization, Alg-R exploits the sparsity of the channel model proposed in [8]; the complexity of the proposed iterative equalizer depends on an integer parameter, denoted S and quantifying the sparsity of the channel model[28].

IV. NUMERICAL RESULTS

Extensive computer simulations have been run to compare Alg-R, MTEE and Alg-W from two different perspectives. In fact, on the one hand, we have assessed their ability to accurately estimate the inner structure of the communication channel and, in particular, to estimate the delays and Doppler shifts characterizing its paths. This issue is relevant not only for digital communications, but also for sensing in JCAS systems. On the other hand, we have evaluated the error performance achievable on different doubly selective channels when the considered algorithms are used for channel estimation and the resulting estimates are exploited for channel equalization. Ensuring a fair comparison between the considered algorithms has required adapting Alg-R and Alg-W to the considered scenarios. More specifically, the following choices have been made in the implementation of these last two algorithms:

1) The same pilot symbol configuration as MTEE has been adopted; this involves N_{pil} pilot channel symbols. In Section III we have mentioned that, if the guardbands surrounding pilot symbols are of proper size, the use of multiple pilots is a viable way to improve the quality of the matrix $\hat{\mathbf{H}}_{\mathrm{w}}$ (144), which can be processed for the acquisition of full CSI.

2) A 2D *spline* interpolation technique[29] has been employed in Alg-R to increase the number of rows of the matrix $\hat{\mathbf{H}}_{\mathrm{w}}$ (144) and that of its columns from P and Q to P_0 and Q_0, respectively. This improves channel estimation accuracy by enhancing the resolution in both the delay and Doppler domains.

---

[26]The overall number of derivatives to be computed is equal to 12; the matrices corresponding to the derivatives of order $(0,3)$, $(3,0)$ and $(3,3)$ of the SDFT of $\hat{\mathbf{h}}_{\mathrm{w}}$ are not needed (see [18, Sec. III.A]).

[27]In the following, the interpolation orders employed for the rows and columns of the spectrum and its derivatives are denoted I_p and I_q, respectively [18, Algorithm 1, Refinement Step].

[28]Note that S is usually greater than L.

[29]In our simulations, the MatlabR2023b *spline* 2D interpolation has been adopted. The interpolation orders adopted for the rows and the columns of the matrix $\hat{\mathbf{H}}_{\mathrm{w}}$ are denoted I_p and I_q, respectively.

3) In Alg-R, the matrix $\hat{\mathbf{H}}_{\mathrm{w}}$ has been processed to detect its L most relevant amplitude peaks (that are associated with relevant normalized delays and Doppler shifts); this is conceptually similar to the peak search in a 2D *periodogram* (e.g., see [27, Sec.IV-A]).

4) In Alg-W, sensing consists of the following two consecutive steps: a) Alg-R is run on the matrix $\hat{\mathbf{H}}_{\mathrm{w}}$ (144) to detect its L most relevant peaks, whose indices are collected in the set $\{(\hat{p}_l, \hat{q}_l); l = 0, 1, ..., L - 1\}$; b) a serial refinement procedure, based on the matrix $\hat{\mathbf{h}}_{\mathrm{w}}$ (143), is accomplished for each peak $(\hat{p}_l, \hat{q}_l)$. This procedure can be repeated up to N_{it} times for each detected peak and closely follows what is described in [16, Algorithm 2], where the input parameters $\tilde{X}_n^{(p)}[l]$, $(\tilde{l}_p, \tilde{n}_p)$ and N_{iter} are replaced by the element (p', q') (with $p' = 0, 1, ..., P - 1$ and $q' = 0, 1, ..., Q - 1$) of $\hat{\mathbf{h}}_{\mathrm{w}}$, the couple of indices $(\hat{p}_l, \hat{q}_l)$ and the number of iterations to be accomplished in each refinement step (i.e., N_{it}), respectively.

5) The MMSE equalizer described in Paragraph III-B (see **E1**-**E3**) has been also employed by Alg-R and Alg-W.

In our simulations, three different scenarios, denoted **SC1**, **SC2** and **SC3**, have been considered. The **first scenario** is characterized by a single path (corresponding to the presence of a single target in sensing), i.e., by $L = 1$. The path amplitude is set to unity, whereas both its delay and Doppler frequency are generated randomly to ensure that their fractional parts are usually different from zero (see comments below (134) and (135)). In sensing, the path delay τ_0 and Doppler shift ν_0 can be easily related to target range R_0 and velocity v_0 as $\tau_0 = 2R_0/c$ and $\nu = 2f_c v_0/c$, respectively (here, f_c and c denote the carrier frequency and the speed of light, respectively). In our simulations, R_0 and v_0 are generated in an independent fashion and are uniformly distributed in $[R_{\min}, R_{\max}]$ and $[v_{\min}, v_{\max}]$, respectively, with $R_{\min} = 0$, $R_{\max} = 30$ m, $v_{\min} = -50$ km/h and $v_{\max} = 50$ km/h.

The **second scenario**, instead, is characterized by a couple of paths having unitary amplitude. The range R_0 and the speed v_0 characterizing the first path are generated in the same way as the corresponding parameters defined for **SC1**; however, $R_{\max} = 26$ m, $v_{\min} = -90$ km/h and $v_{\max} = 90$ km/h have been selected. The range R_1 and the velocity v_1 characterizing the second path are evaluated as

$$R_1 = R_0 + (3 + \rho_{\mathrm{r}})R_{\mathrm{bin}} \tag{149}$$

and

$$v_1 = v_0 + (3 + \rho_{\mathrm{v}})v_{\mathrm{bin}}, \tag{150}$$

respectively; here, $R_{\mathrm{bin}} = \mathrm{c}/(2M\Delta_f)$ and $v_{\mathrm{bin}} = \mathrm{c}/(2NT_s f_c)$ are the *bin resolutions* for range and velocity, respectively, whereas ρ_{r}, and ρ_{v} are independent random parameters and each of them is uniformly distributed between 0 and 0.5.

The **third scenario** is characterized by three paths, all having unitary amplitude. In this case, the range R_0 characterizing the first path is generated in the same way as the corresponding parameter defined for **SC1**; however, $R_{\max} = 25$ m has been chosen. On the other hand, the ranges characterizing the other two paths have been generated as

$$R_l = R_0 + l\bar{R}R_{\mathrm{bin}}, \tag{151}$$

with $l = 1$ and 2; in our simulations, the parameter $\bar{R}$, that represents the bin spacing for the normalized range, has been always set to 2. The velocities associated with the considered paths have been generated according to the Jake's formula (e.g., see [8]), that is as

$$v_l = v_{\max} \cos(\theta_l), \tag{152}$$

with $l = 0, 1$ and 2; here, $v_{\max} = 250$ km/h and θ_l is a random parameter uniformly distributed over $[-\pi, \pi]$.

The selection of the three scenarios defined above can be motivated as follows. The first scenario allows us to assess the performance of the considered algorithms in the absence of interference between different paths; in this case, the spectral leakage affecting pilot symbols originates from data symbols. In the second scenario, the contributions due to the couple of paths are adequately spaced in the DD domain (since the spacing corresponds to 3 resolution bins for both range and velocity), but leakage has a random impact because of the presence of the terms ρ_{r} and ρ_{v} in (149) and (150), respectively; this makes the task of channel estimation harder. Finally, in the third scenario, the overall number of paths is larger than that of the other two and Doppler shifts are randomly distributed according to the widely adopted Jake's spectrum (e.g., see [6, Example 2.2.8]). This last scenario allows us to assess how the considered algorithms perform when we use: a) a couple of pilots; b) a single pilot surrounded
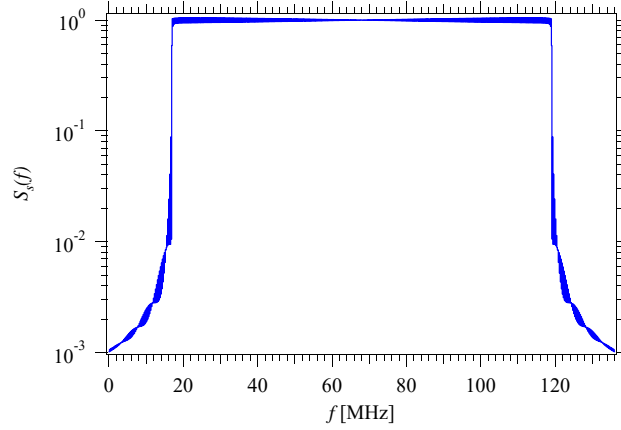
Fig. 7. Normalized PSD of an OTFS signal characterized by the following parameters: 1) $\Delta_f = 250$ kHz, $M = N = 512$, $N_{cp}^{(FD)} = N_{cpo}^{(FD)} = 16$, $N_{cp}^{(TD)} = 16$, $T_s = 1/\Delta_f$ and $\alpha = 0.25$.

by a guard wide enough to accommodate a Doppler shift corresponding to twice its maximum value (with the aim of mitigating the impact of leakage).

In our computer simulations, the following parameters have been selected for the OTFS modulation: 1) $M = 512$ and $N = 512$ for the data matrix $\mathbf{C}$; 2) frequency spacing $\Delta_f = 250$ kHz; 3) TD cyclic prefix size $N_{cp}^{(TD)} = N/32$; 4) FD cyclic prefix and post-fix sizes $N_{cp}^{(FD)} = N_{cpo}^{(FD)} = M/32$; 5) carrier frequency $f_c = 24$ GHz; 6) roll-off factor for the RRC pulse $\alpha = 0.25$; 7) gain tolerance adopted in the evaluation of the overall number of SCs $\varepsilon = 0.05$; 8) cardinality of the PSK modulation $M_c = 4$ (Gray coding is used in symbol mapping).

The choice of these parameters entails that: 1) $T_s = 1/\Delta_f = 4$ µs; 2) the bin sizes along range and velocity are $R_{\text{bin}} = 1.17$ m and $v_{\text{bin}} = 3.05$ m/s, respectively; 3) the percentage of overhead due to the insertion of the DCP is 8.73% (see (62)). The PSD (127) for the considered DCP-OTFS modulation format, normalized with respect to

$$\frac{1}{NT_s}\frac{\sigma_c^2}{N + N_{cp}^{(TD)}}, \tag{153}$$

is shown in Fig. 7. Note that the bandwidth of the transmitted signal is approximately given by $B_s = 136$ MHz (see (130)) and that the most significant part of the spectral content is contained in the frequency range $[20, 120]$ MHz.

As far as the transmission of pilot symbols is concerned, the use of a variable number of pilot symbols (in particular, $N_{\text{pil}} \in \{1, 2, 3, 4\}$) has been considered in the first two scenarios. In all cases, the guard of each pilot is generated according to the criterion expressed by (131). Moreover, the guard parameters $p_\tau = 26$ and $q_\nu = 5$ have been adopted in **SC1** (so that $P = 27$ and $Q = 11$), and $p_\tau = 26$ and $q_\nu = 12$ in **SC2** (so that $P = 27$ and $Q = 25$). Note that the values of p_τ and q_ν have been selected according to (134) and (135), respectively. In **SC3**, instead, the guard size is the same as **SC2** when two pilots are employed; however, $q_\nu = 24$ has been selected in the case of a single pilot, in order to double the guard size along Doppler direction.

Our computer simulations have aimed at assessing: a) the *bit error rate* (BER) achieved by the OTFS-based communication represented in Fig. 1 when each of the considered algorithms is used at its RX side; b) the *root mean square error* (RMSE) achieved in range (RMSE$_R$) and velocity (RMSE$_v$) estimation by each of the considered algorithms. Note that the first performance index is meaningful in data communication only, whereas the last two are also relevant for sensing applications. In generating our numerical results concerning the performance indices mentioned above, the following choices have been made for all the compared algorithms:

1) The oversampling factors $N_p = N_q = 16$ have been adopted for all the algorithms (so that $P_0 = N_p P = 432$ for all scenarios, whereas $Q_0 = N_q Q = 176$ and 400 in **SC1** and **SC2/SC3**, respectively).

2) The overall number of paths (L) has been assumed to be known at the RX side.

3) In the MTEE algorithm, $N_{\text{it}} = 5$ refinement steps have been accomplished for the computation of the normalized delay and Doppler residuals, the interpolation orders $I_p = I_q = 7$ have been selected, and $N_{\text{ref}} = 2$ re-estimations have been executed.
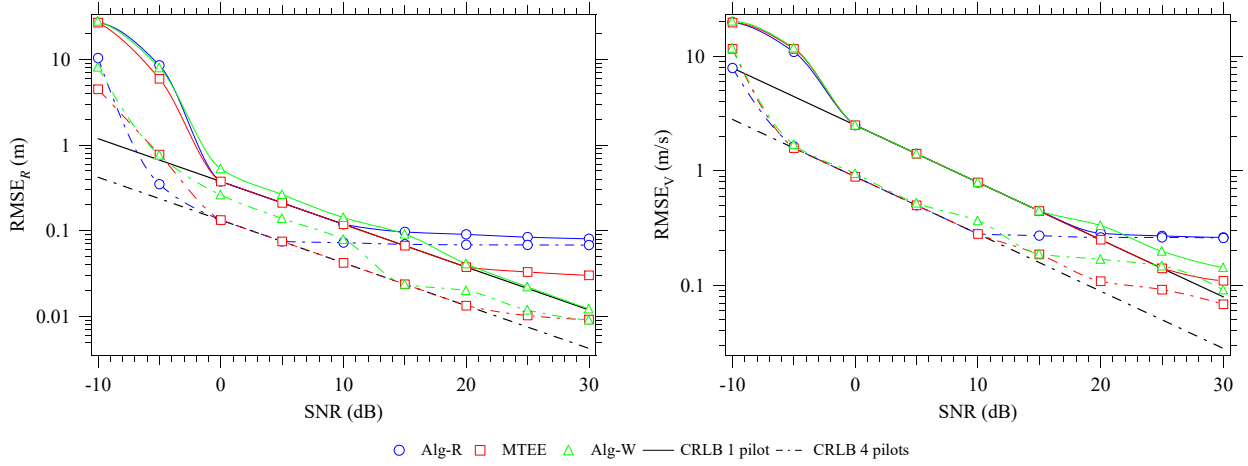
Fig. 8. Root mean square error performance achieved by Alg-R, the MTEE algorithm and Alg-W in range (left figure) and velocity estimation (right figure) in the first scenario. The CLRB is also shown.
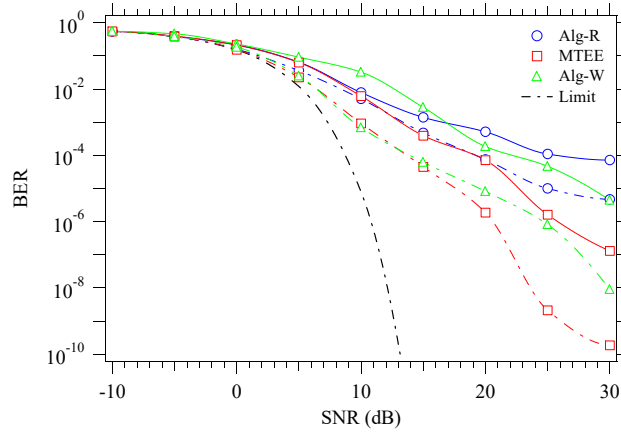

Fig. 9. Bit error rate performance achieved by Alg-R, the MTEE algorithm and Alg-W in the first scenario.

4) In Alg-W, $N_{\mathrm{it}} = 5$ refinement steps have been executed.

5) The noise variance σ^2 has been assumed to be known in all the considered scenarios; consequently, $\hat{\sigma}^2 = \sigma^2$ has been adopted for the evaluation of the term $G_{\mathrm{mmse}}[\tilde{k}, \tilde{n}]$ (145), employed during the equalization step of each algorithm.

Our numerical results are illustrated in the following figures. In analyzing them, readers should keep in mind that:

1) Simulation results are represented by labels, whereas solid and dashed lines are drawn to ease reading.

2) In all the figures referring to **SC1** and **SC2**, solid lines refer to the transmission of a single pilot for channel estimation, whereas dashed lines refer to the transmission of 4 pilots in the same OTFS symbol.

3) In the evaluation of the SNR, we have taken into account the energy loss originating from the presence of one or more pilot symbols, but not that due to the use of a DCP for simplicity (this would result in an SNR loss equal to 0.085 dB).

Some numerical results referring to **SC1** are illustrated in Figs. 8 and 9. In particular, the $\mathrm{RMSE}_{\mathrm{R}}$ and $\mathrm{RMSE}_{\mathrm{v}}$ characterizing all the considered algorithms are shown for an SNR $\in [-10, 30]$ dB; the *Cramér-Rao lower bound*[30] (CRLB) is also provided as a reference. The BER performance achievable in the same SNR range through the use of all the considered algorithms is shown in Fig. 9. Moreover, in that figure, the BER performance achieved by the coherent demodulation of an uncoded QPSK over an AWGN channel is also shown (see [28, Subsect. 5.2.7, eq. (5.2.59)]), since it provides a lower bound.

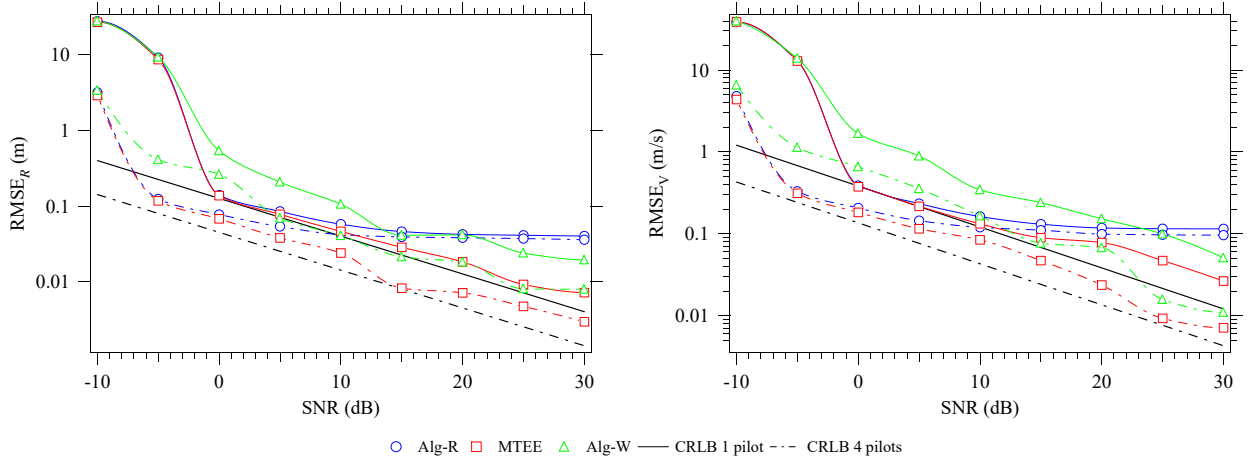[30]The evaluation of this bound is based on the methodology described in [27, App. A].

Fig. 10. Root mean square error performance achieved by Alg-R, the MTEE algorithm and Alg-W in range (left figure) and velocity estimation (right figure) in the second scenario. The CLRB is also shown.
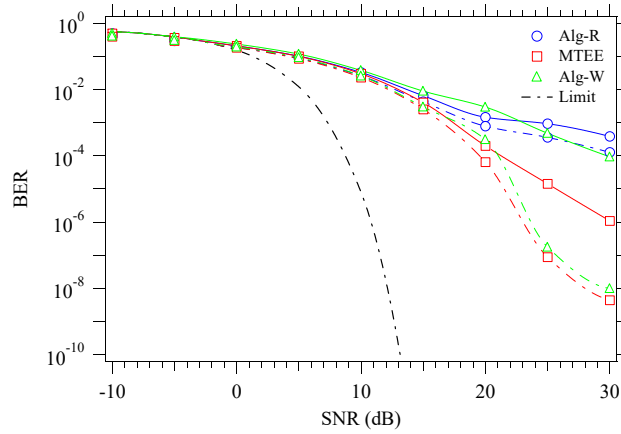

Fig. 11. Bit error rate performance achieved by Alg-R, the MTEE algorithm and Alg-W in the second scenario.

The results shown in Figs. 8 and 9 lead to the following conclusions:

1) An SNR *threshold* can be easily identified in all the RMSE curves; in all cases, the threshold is lowered by an increase of the number of pilot symbols from one to four.

2) All the techniques exhibit an RMSE *floor* at high SNRs. This is due to the fact that Alg-R does not include a refinement step and limits its estimation to peak searching on the matrix $\hat{\mathbf{H}}_{\text{w}}$ (144). Conversely, for the other two techniques, their refinement step relies on the input matrix $\hat{\mathbf{h}}_{\text{w}}$ (143), which ideally should represent a pure overlap of 2D complex exponentials (this condition is perfectly met in the FG case only).

3) The MTEE algorithm achieves the best estimation accuracy in terms of RMSE_{v}, whereas Alg-W achieves it in terms of RMSE_{R} at high SNRs. This can be related to the fact that Alg-W refinement step converges faster, provided that the 2D tones are adequately spaced.

4) Alg-R and the MTEE algorithm offer the worst and the best BER performance, respectively. Note also that Alg-W is outperformed by Alg-R for an SNR $\in [5, 20]$ dB. This can be related to the fact Alg-R achieves an RMSE_{v} lower than that of Alg-W in the considered SNR range.

It is also worth mentioning that:

1) The computational complexity for the sensing steps of Alg-W and the MTEE algorithm is 1.1 and 13.1 times higher than that of Alg-R, respectively (see Table I). Even if the MTEE algorithm exhibits a higher complexity (this is due to its initialization cost), it achieves a better complexity-performance trade-off than the other two methods.

2) The percentages of transmission rate loss Λ_{pil} (138) due to pilots in **SC1** are 0.44% and 1.76% for 1 and 4 pilots, respectively.
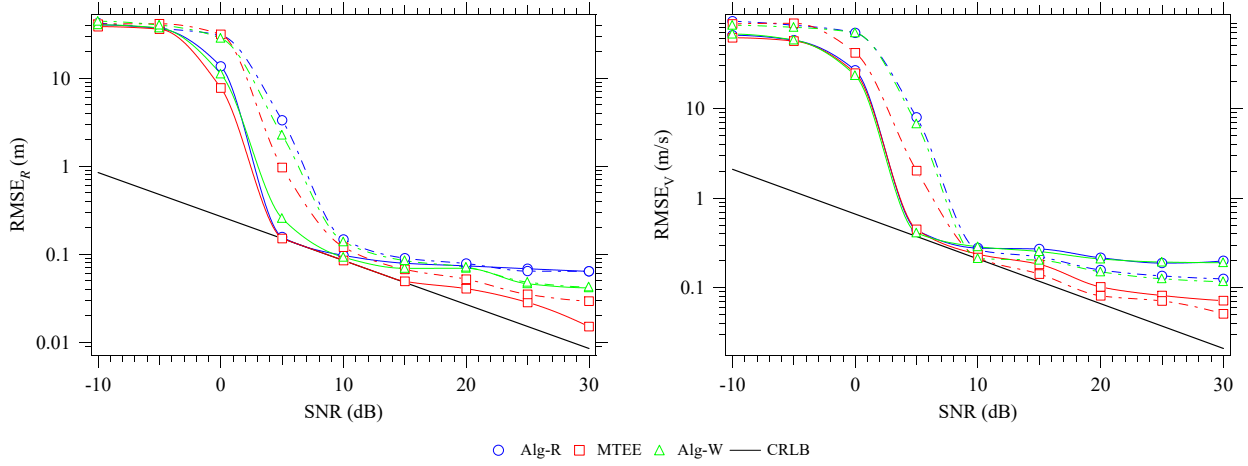
Fig. 12. Root mean square error performance achieved by Alg-R, the MTEE algorithm and Alg-W in range (left figure) and velocity estimation (right figure) in the third scenario.
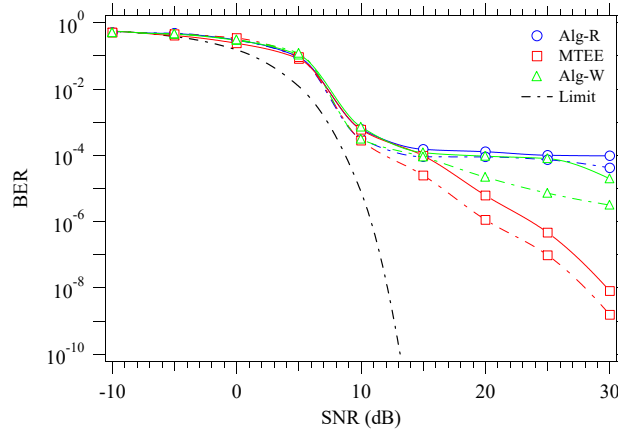

Fig. 13. Bit error rate performance achieved by Alg-R, the MTEE algorithm and Alg-W in the third scenario.

Some numerical results referring to the RMSE performance and the BER performance achieved in **SC2** are shown in Figs. 10 and 11, respectively. From these results it can be inferred that:

1) The MTEE algorithm achieves the best accuracy in terms of both range and velocity estimation. This improvement is mainly due to the *serial cancellation* mechanism adopted by the CSFDEC algorithm.

2) Similarly as **SC1**, estimation accuracy improves as the overall number of pilots increases. However, the performance gap between the considered techniques is significantly larger than that observed in **SC1**. This is due to the presence of multiple paths, whose fractional delays and Doppler frequencies generate a stronger leakage (i.e., interference) that affects not only pilots but also data symbols.

3) The BER performance of all the algorithms is worse than that observed in **SC1**. Moreover, Alg-R is outperformed by the other two techniques and exhibits an high floor even when four pilots are used.

It is also important to point that:

1) The computational complexity of the sensing step of Alg-W and the MTEE algorithm is 1.1 and 13.1 times higher than that of Alg-R, respectively (see Table I) as in **SC1**; for this reason, the considerations illustrated for that scenario also apply to **SC2**.

2) The percentages of transmission rate loss Λ_{pil} (138) due to pilots in **SC2** are 1% and 4% for 1 and 4 pilots, respectively.

Our last numerical results, referring to **SC3**, are illustrated in Figs. 12 and 13. In these figures, solid lines refer to the case in which two pilot symbols are used, whereas dashed lines refer to the use of a single pilot with a guard size doubled along the Doppler direction. The last results evidence that:

1) All the algorithms exhibit similar thresholds in their RMSE performance. If one or two pilots are used, the SNR threshold is approximately 6 dB and 10 dB, respectively.

2) An high floor is visible in the RMSE_R and RMSE_v curves referring to Alg-R.

3) Alg-W performs better than Alg-R in terms of RMSE_R, whereas its performance in terms of RMSE_v is comparable to that achieved by Alg-W.

4) The MTEE algorithm performs substantially better than all the other algorithms for high SNRs (more precisely, for SNR ≥ 15 dB).

5) Increasing the guard size along the Doppler dimension improves the estimation accuracy in terms of RMSE_v. On the contrary, the use of two pilots with smaller guard size along the Doppler dimension improves RMSE_R.

6) The BER performance achieved in the case of a single pilot with a double guard size is better than that obtained with a couple of pilots. This is mainly due to the fact that **SC3** is characterized by a significant Doppler spread. On the other hand, the delay has a weaker impact, even if it introduces some leakage.

Note that, the percentage of transmission rate loss Λ_pil (138) is 2% in both the cases considered in **SC3**.

Finally, based on all the results illustrated above, we can state that: a) the proposed modulation format, based on an OTFS modulation incorporating a DCP and on the selection of a proper pulse shape, can be considered as a good candidate for future JCAS systems; b) the MTEE algorithm outperforms all the considered technical alternatives over doubly selective fading channels thanks to its ability to accurately estimate fractional delays and Doppler shifts; c) the performance improvement provided by the MTEE algorithm is obtained at the price of a limited complexity increase with respect to other methods.

V. CONCLUSIONS

In this manuscript, a novel modulation format, resulting from the insertion of a DCP in the OTFS modulation, has been proposed. The impact of pulse shaping on the inner structure of the modulated signal has been analyzed and a specific proposal for pulse selection has been made. Moreover, a receiver architecture for the considered modulation format has been described and a novel algorithm for pilot-aided channel estimation, dubbed MTEE, has been developed. Our numerical results have evidenced that the MTEE algorithm is able to estimate the inner structure of a multipath communication channel with a better accuracy then other technical alternatives at the price of a limited complexity. For this reason, it represents a good technical solution for OTFS-based JCAS systems in which channel estimation is needed at the TX side for sensing and at the RX side of another device for channel equalization. Our future research activities concern 1) the implementation of the proposed OTFS-DCP system on real hardware and 2) the development of novel algorithms for channel estimation & equalization to be employed during the transmission of multiple OTFS symbols in the presence of doubly selective fading channels.

APPENDIX

A. Derivation of the Fourier coefficients of the transmitted OTFS signal

In this appendix, the expression (70) of the coefficients $S_{k,q}^{(\text{TD})}(\mathbf{C})$ is derived. To begin, we substitute the RHS (65) in that of (69); this produces

$$S_{k,q}^{(\text{TD})}(\mathbf{C}) \triangleq \frac{1}{T} \sum_{l=-\infty}^{+\infty} x_{k,l} \int_0^T p(t - lT_s) \cdot \exp\big(j2\pi k \Delta_f (t - lT_s)\big) \exp\left(-j2\pi q \frac{t}{T}\right) dt. \tag{154}$$

The last formula can be rewritten as

$$S_{k,q}^{(\text{TD})}(\mathbf{C}) \triangleq \frac{1}{T} \sum_{n=0}^{N-1} x_{k,n} \sum_{l'=-\infty}^{+\infty} \int_0^T p(t - (n + l'N)T_s) \cdot \exp\big(j2\pi k \Delta_f t\big) \exp\left(-j2\pi q \frac{t}{T}\right) dt, \tag{155}$$

where $l = n + l'N$, $n = 0, 1, ..., N-1$ and l' is an arbitrary integer; moreover, $T_s = 1/\Delta_f$. Replacing the variable t with $t' \triangleq t - (n + l'N)T_s$ in the RHS of the last formula yields, after some straightforward manipulation,

$$S_{k,q}^{(\text{TD})}(\mathbf{C}) = \frac{1}{\sqrt{N}T_s} X_{k,q} \sum_{l'=-\infty}^{+\infty} \int_{-(n+l'N)T_s}^{-(n+(l'-1)N)T_s} p(t') \cdot \exp\left(-j2\pi \left(\frac{q - kN}{T}\right) t'\right) dt', \tag{156}$$

where $X_{k,q}$ is expressed by (71). Since the sum over l' in (156) involves the integration interval only, that equation can be rewritten as

$$S_{k,q}^{(\mathrm{TD})}(\mathbf{C}) = \frac{X_{k,q}}{\sqrt{N}T_s} \int_{-\infty}^{+\infty} p(t) \exp\left(-j2\pi\left(\frac{q-kN}{T}\right)t\right) dt, \tag{157}$$

if the variable t is used in place of t'. The integral in the last formula represents the FCT of $p(t)$ (i.e., $P(f)$; see (8)) evaluated at the frequency $f = (q-kN)/T$. Therefore, (70) can be easily inferred from (157).

B. Derivation of the received OTFS signal model in the presence of an ideal communication channel

In this appendix, the expression of the OTFS signal model $r[\tilde{k}, \tilde{n}]$ (80) is derived. First of all, we substitute the RHS of (77) in that of (79); this yields

$$r[\tilde{k}, \tilde{n}] = \frac{1}{\sqrt{N}} \sum_{q=0}^{N-1} \left[\sum_{k=-\infty}^{+\infty} X_{k,q} \hat{G}_{\tilde{k}-k,q}\right] \exp\left(j2\pi\frac{q}{N}\tilde{n}\right). \tag{158}$$

In the last formula, the inner sum can be interpreted, for a given q, as the response, at the $\tilde{k}$th instant, of a discrete-time linear filter, having *impulse response* $\{\hat{G}_{k,\cdot}\}$, to the periodic sequence $\{X_{k,\cdot}\}$ (whose period is equal to M). Therefore, it can be expressed as (e.g., see [29, Sec. 7.6.2, eq. (7.28)])

$$\sum_{k=-\infty}^{+\infty} X_{k,q} \hat{G}_{\tilde{k}-k,q} = \frac{1}{\sqrt{M}} \sum_{p=0}^{M-1} \bar{X}_{p,q} \bar{g}_{p,q} \exp\left(-j2\pi\frac{p}{M}\tilde{k}\right), \tag{159}$$

where $\bar{X}_{p,q}$ and $\bar{g}_{p,q}$ are defined in (81) and (82), respectively. Substituting the RHS of (159) in that of (158) yields (80).

C. Derivation of the OTFS signal model at the RX side in the presence of a doubly selective fading channel

In this appendix, the expression of the OTFS signal model $r_l[\tilde{k}, \tilde{n}]$ (106) is derived. To begin, we reformulate (101) replacing the index q appearing in it with $\tilde{q} \triangleq q - \tilde{k}N$; this produces

$$r_{k,l}[\tilde{k}, \tilde{n}] = \frac{A_l}{\sqrt{N}} \exp\left(-j2\pi\tilde{k}F_{\tau_l}\right) \exp\left(j2\pi\tilde{n}F_{\nu_l}\right) \cdot \sum_{\tilde{q}=-\infty}^{+\infty} X_{k,\tilde{q}} G_{\tilde{k}-k,\tilde{q},l} \exp\left(-j2\pi\frac{\tilde{q}}{N}F_{\tau_l}\right) \exp\left(j2\pi\frac{\tilde{q}}{N}\tilde{n}\right), \tag{160}$$

where

$$G_{x,\tilde{q},l} \triangleq \frac{1}{T_s} P\left(\frac{\tilde{q}+xN}{T}\right) P^*\left(\frac{\tilde{q}+F_{\nu_l}N}{T}\right). \tag{161}$$

Then, we replace the index $\tilde{q}$ with the couple of indices (q, u) such that $\tilde{q} \triangleq q + uN$, with $q = 0, 1, ..., N-1$ and u arbitrary integer; this yields

$$r_{k,l}[\tilde{k}, \tilde{n}] = \frac{A_l}{\sqrt{N}} \exp\left(-j2\pi\tilde{k}F_{\tau_l}\right) \exp\left(j2\pi\tilde{n}F_{\nu_l}\right) \cdot \sum_{q=0}^{N-1} X_{k,q} \hat{G}_{\tilde{k}-k,q}(F_{\tau_l}, F_{\nu_l}) \exp\left(j2\pi\frac{q}{N}\tilde{n}\right), \tag{162}$$

where

$$\hat{G}_{x,q}(F_{\tau_l}, F_{\nu_l}) \triangleq \sum_{u=-\infty}^{+\infty} G_{x,q,l} \exp\left(-j2\pi\frac{q+uN}{N}F_{\tau_l}\right)$$

$$= \frac{1}{T_s} \sum_{u=-\infty}^{+\infty} P\left(\frac{q+(u+x)N}{T}\right) \cdot P^*\left(\frac{q+(u+F_{\nu_l})N}{T}\right) \exp\left(-j2\pi\frac{(q+uN)}{N}F_{\tau_l}\right) \tag{163}$$

represents the counterpart of the quantity $\hat{G}_{x,q}$ (78) defined for the case of an ideal channel; note, however, that, unlike $\hat{G}_{x,q}$, $\hat{G}_{x,q}(F_{\tau_l}, F_{\nu_l})$ depends not only on the pulse spectrum $P(f)$, but also on the normalized delay F_{τ_l} and the normalized Doppler frequency F_{ν_l}.

Equation (162) describes the contribution given to the output of the $\tilde{k}$th RX filter by the lth path of the communication channel fed by the kth component of $s(t; \mathbf{C})$ (64). The contribution of all the components of the last signal can be accounted for by summing over the index k (see (64)); this produces

$$r_l[\tilde{k}, \tilde{n}] \triangleq \sum_{k=-(M/2+N_{cp}^{(FD)})}^{M/2-1+N_{cpo}^{(FD)}} r_{k,l}[\tilde{k}, \tilde{n}], \tag{164}$$

which can be rewritten as

$$r_l[\tilde{k}, \tilde{n}] \triangleq \sum_{k=-\infty}^{+\infty} r_{k,l}[\tilde{k}, \tilde{n}], \tag{165}$$

thanks to the assumptions made on the cyclic structure of the transmitted signal. Then, substituting the RHS of (162) in that of the last equation yields

$$r_l[\tilde{k}, \tilde{n}] = \frac{A_l}{\sqrt{N}} \exp\left(-j2\pi\tilde{k}F_{\tau_l}\right) \exp\left(j2\pi\tilde{n}F_{\nu_l}\right) \cdot \sum_{q=0}^{N-1}\left[\sum_{k=-\infty}^{+\infty} X_{k,q}\, \hat{G}_{\tilde{k}-k,q}(F_{\tau_l}, F_{\nu_l})\right] \exp\left(j2\pi\frac{q}{N}\tilde{n}\right). \tag{166}$$

The last expression contains the convolution

$$\sum_{k=-\infty}^{+\infty} X_{k,q}\, \hat{G}_{\tilde{k}-k,q}(F_{\tau_l}, F_{\nu_l}), \tag{167}$$

that can be interpreted as the response, at the $\tilde{k}$th instant, of a discrete-time linear filter, having impulse response $\{\hat{G}_{k,\cdot}(F_{\tau_l}, F_{\nu_l})\}$, to the periodic sequence $\{X_{k,\cdot}\}$ (whose period is equal to M). Then, following the same line of reasoning as that illustrated for the derivation of (159), (166) can be easily reformulated as (106).

D. Power spectral density of OTFS modulation

In this appendix, the derivation of (127)-(128) is sketched. Our mathematical developments rely on the model (64), representing the complex envelope (63) of an OTFS signal as the superposition of the signals of the set

$$\mathcal{S}^{(TD)} \triangleq \{s_k^{(TD)}(t; \mathbf{C}); \ k = -M/2 + N_{cp}^{(FD)}, -M/2 + N_{cp}^{(FD)} + 1, ..., M/2 - 1 + N_{cpo}^{(FD)}\}, \tag{168}$$

with (see (65))

$$s_k^{(TD)}(t; \mathbf{C}) \triangleq \sum_{l=-N_{cp}^{(TD)}}^{N-1} x_{k,l}\, p(t - lT_s) \exp\left(j2\pi k\Delta_f(t - lT_s)\right) \tag{169}$$

for any k. Note also that $s_k^{(TD)}(t; \mathbf{C})$ represents the frequency-shifted version of the complex envelope of an OFDM signal (the frequency shift is given by $k\Delta_f$, that also represents the central frequency of that signal). In our derivations we assume that:

1) The useful elements[31] $\{c_{m,n}\}$ of the channel symbol matrix $\mathbf{C}$ have the following properties: a) they belong to an $M_c$ary constellation; b) they are statistically independent and identically distributed (in particular, they have zero mean and variance σ_c^2). The last assumption implies that the channel symbols $\{x_{k,l}\}$ are also statistically independent and identically distributed thanks to the *orthogonality* property of the SDFT transform (see (92)).

2) The spectrum $P(f)$ of the pulse $p(t)$ appearing in the RHS of (169) is expressed by (17).

Based on these assumptions, it can be proved that the *cross-correlation* function

$$R_{k,m} \triangleq \mathrm{E}\left[s_{k+m}^{(TD)}(t; \mathbf{C})(s_k^{(TD)}(t; \mathbf{C}))^*\right] \tag{170}$$

is equal to zero for any $m \neq 0$, so that all the signals of the set $\mathcal{S}^{(TD)}$ (168) are *statistically uncorrelated*. Consequently the PSD of $s(t; \mathbf{C})$ (64) can be expressed as the superposition of the PSD of all the signals of $\mathcal{S}^{(TD)}$, i.e., as in (127). Moreover, for any $k \neq 0$, the PSD $S_{s_k}(f)$ of $s_k^{(TD)}(t; \mathbf{C})$ can be obtained from that of $s_0^{(TD)}(t; \mathbf{C})$ by introducing a simple frequency shift. Since $s_0^{(TD)}(t; \mathbf{C})$ represents the complex envelope of an OFDM signal (see (65)), its PSD is expressed by [6, Subsect. 3.7.3.3, eq. (3.295)]. These considerations lead easily to (128). $\square$

---

[31] Do not forget that a portion of the elements of $\mathbf{C}$ is set to zero.

References

[1] D. K. Pin Tan, J. He, Y. Li, A. Bayesteh, Y. Chen, P. Zhu, and W. Tong, "Integrated Sensing and Communication in 6G: Motivations, Use Cases, Requirements, Challenges and Future Directions," in *2021 1st IEEE International Online Symposium on Joint Communications & Sensing (JC&S)*, 2021, pp. 1–6.

[2] Z. Wei, H. Qu, Y. Wang, X. Yuan, H. Wu, Y. Du, K. Han, N. Zhang, and Z. Feng, "Integrated Sensing and Communication Signals Toward 5G-A and 6G: A Survey," *IEEE Internet Things J.*, vol. 10, no. 13, pp. 11 068–11 092, 2023.

[3] F.-M. Han and X.-D. Zhang, "Wireless multicarrier digital transmission via weyl-heisenberg frames over time-frequency dispersive channels," *IEEE Trans. Commun.*, vol. 57, no. 6, pp. 1721–1733, Jun. 2009.

[4] R. Hadani, S. Rakib, M. Tsatsanis, A. Monk, A. J. Goldsmith, A. F. Molisch, and R. Calderbank, "Orthogonal Time Frequency Space Modulation," in *2017 IEEE Wireless Communications and Networking Conference (WCNC)*, Mar. 2017, pp. 1–6.

[5] R. Hadani and A. Monk, "OTFS: A New Generation of Modulation Addressing the Challenges of 5G," Feb. 2018.

[6] G. M. Vitetta, D. P. Taylor, G. Colavolpe, F. Pancaldi, and P. A. Martin, *Wireless communications: algorithmic techniques*. John Wiley & Sons, 2013.

[7] P. Bello, "Time-frequency duality," *IEEE Trans. Inf. Theory*, vol. 10, no. 1, pp. 18–33, Jan. 1964.

[8] P. Raviteja, K. T. Phan, and Y. Hong, "Embedded Pilot-Aided Channel Estimation for OTFS in Delay–Doppler Channels," *IEEE Trans. Veh. Technol.*, vol. 68, no. 5, pp. 4906–4917, May 2019.

[9] P. Raviteja, Y. Hong, E. Viterbo, and E. Biglieri, "Practical Pulse-Shaping Waveforms for Reduced-Cyclic-Prefix OTFS," *IEEE Trans. Veh. Technol.*, vol. 68, no. 1, pp. 957–961, Jan. 2019.

[10] S. K. Mohammed, "Derivation of OTFS Modulation From First Principles," *IEEE Trans. Veh. Technol.*, vol. 70, no. 8, pp. 7619–7636, Aug. 2021.

[11] L. Xiao, S. Li, Y. Qian, D. Chen, and T. Jiang, "An Overview of OTFS for Internet of Things: Concepts, Benefits, and Challenges," *IEEE Internet Things J.*, vol. 9, no. 10, pp. 7596–7618, May 2022.

[12] P. Raviteja, K. T. Phan, Y. Hong, and E. Viterbo, "Interference Cancellation and Iterative Detection for Orthogonal Time Frequency Space Modulation," *IEEE Trans. Wireless Commun.*, vol. 17, no. 10, pp. 6501–6515, Aug. 2018.

[13] L. Gaudio, M. Kobayashi, G. Caire, and G. Colavolpe, "On the Effectiveness of OTFS for Joint Radar Parameter Estimation and Communication," *IEEE Trans. Wireless Commun.*, vol. 19, no. 9, pp. 5951–5965, Sep. 2020.

[14] A. Janssen, "The Zak transform: A signal transform for sampled time-continuous signals," *Philips Journal of Research*, vol. 43, Jan. 1988.

[15] P. Singh, S. Tiwari, and R. Budhiraja, "Low-Complexity LMMSE Receiver Design for Practical-Pulse-Shaped MIMO-OTFS Systems," *IEEE Trans. Commun.*, vol. 70, no. 12, pp. 8383–8399, Dec. 2022.

[16] K. Wu, J. A. Zhang, X. Huang, and Y. J. Guo, "OTFS-Based Joint Communication and Sensing for Future Industrial IoT," *IEEE Internet Things J.*, vol. 10, no. 3, pp. 1973–1989, Feb. 2023.

[17] X. Wang, X. Shi, J. Wang, and J. Song, "On the Doppler Squint Effect in OTFS Systems Over Doubly-Dispersive Channels: Modeling and Evaluation," *IEEE Trans. Wireless Commun.*, vol. 22, no. 12, pp. 8781–8796, Dec. 2023.

[18] M. Mirabella, P. D. Viesti, A. Davoli, and G. M. Vitetta, "An Approximate Maximum Likelihood Method for the Joint Estimation of Range and Doppler of Multiple Targets in OFDM-Based Radar Systems," *IEEE Trans. Commun.*, vol. 71, no. 8, pp. 4862–4876, Aug. 2023.

[19] W. Abu-Al-Saud and G. Stuber, "Efficient wideband channelizer for software radio systems using modulated PR filterbanks," *IEEE Trans. Signal Process.*, vol. 52, no. 10, pp. 2807–2820, Sep. 2004.

[20] Y. Qiu, Z. Liu, and D. Qu, "Filtered bank based implementation for filtered OFDM," in *2017 7th IEEE International Conference on Electronics Information and Emergency Communication (ICEIEC)*, Jul. 2017, pp. 15–18.

[21] G. D. Surabhi, R. M. Augustine, and A. Chockalingam, "On the Diversity of Uncoded OTFS Modulation in Doubly-Dispersive Channels," *IEEE Trans. Wireless Commun.*, vol. 18, no. 6, pp. 3049–3063, Apr. 2019.

[22] I. A. Khan and S. K. Mohammed, "A Low-Complexity OTFS Channel Estimation Method for Fractional Delay-Doppler Scenarios," *IEEE Wireless Commun. Lett.*, vol. 12, no. 9, pp. 1484–1488, Sep. 2023.

[23] G. D. Surabhi and A. Chockalingam, "Low-Complexity Linear Equalization for OTFS Modulation," *IEEE Commun. Lett.*, vol. 24, no. 2, pp. 330–334, Feb. 2020.

[24] F. Liu, Z. Yuan, Q. Guo, Z. Wang, and P. Sun, "Message Passing-Based Structured Sparse Signal Recovery for Estimation of OTFS Channels With Fractional Doppler Shifts," *IEEE Trans. Wireless Commun.*, vol. 20, no. 12, pp. 7773–7785, Dec. 2021.

[25] L. Gaudio, G. Colavolpe, and G. Caire, "OTFS vs. OFDM in the Presence of Sparsity: A Fair Comparison," *IEEE Trans. Wireless Commun.*, vol. 21, no. 6, pp. 4410–4423, Jun. 2022.

[26] M. Mirabella, P. D. Viesti, A. Davoli, and G. M. Vitetta, "Deterministic Signal Processing Techniques for OFDM-Based Radar Sensing: An Overview," *IEEE Access*, vol. 11, pp. 68 872–68 889, Jul. 2023.

[27] M. Mirabella, P. Di Viesti, and G. M. Vitetta, "Deterministic Algorithms for Four-Dimensional Imaging in Colocated MIMO OFDM-Based Radar Systems," *IEEE Open Journal of the Communications Society*, vol. 4, pp. 1516–1543, Jul. 2023.

[28] J. G. Proakis, *Digital communications*. McGraw-Hill, Higher Education, 2008.

[29] R. Baraniuk, *Signals and systems*. Rice University, 2015.

Michele Mirabella received the BS degree and the MS degree in Electronic Engineering (both cum laude) from the University of Modena and Reggio Emilia (Italy) in 2019 and from the University of Bologna in 2021, respectively. From January 2021, he holds the position of Ph.D student at the University of Modena and Reggio Emilia. His main research interests lie in the area of Joint Communication and Sensing systems.

Pasquale Di Viesti received the Bachelor's and the Master Degree in Electronic Engineering (both cum laude), from the University of Modena and Reggio Emilia, Italy, in 2016 and 2018, respectively. From November 2018 to October 2021, he has been enrolled in the Ph.D. program in "Automotive for an intelligent mobility" at the University of Bologna. He is currently a post-doctoral research Fellow with the University of Modena and Reggio Emilia. His main research interests lie in the area of statistical signal processing and MIMO radars.

Giorgio M. Vitetta received the Dr. Ing. Degree in Electronic Engineering (cum Laude) in 1990 and the Ph. D. degree in 1994, both from the University of Pisa, Italy. He holds the position of Full Professor of Telecommunications at the University of Modena and Reggio Emilia since 2001. His main research interests lie in the broad area of wireless and wired data communications, localization systems, MIMO radars and the smart grid. He has served as an Area Editor of the IEEE Transactions on Communications and as an Associate Editor of the IEEE Wireless Communications Letters and the IEEE Transactions on Wireless Communications. He has co-authored more than 100 papers published on international journals and on the proceedings of international conferences, and has co-authored the book Wireless Communications: Algorithmic Techniques (John Wiley, 2013).